Enhanced Dissipation of Internal Tides in a Mesoscale Baroclinic Eddy

YANG WANG[a,b] AND SONYA LEGG[b]

[a] *Institute of Oceanology, Chinese Academy of Sciences, Qingdao, China*
[b] *Program in Atmospheric and Oceanic Sciences, Princeton University, Princeton, New Jersey*

(Manuscript received 15 March 2023, in final form 11 July 2023, accepted 14 July 2023)

ABSTRACT: The dissipation of low-mode internal tides as they propagate through mesoscale baroclinic eddies is examined using a series of numerical simulations, complemented by three-dimensional ray tracing calculations. The incident mode-1 internal tide is refracted into convergent energy beams, resulting in a zone of reduced energy flux in the lee of the eddy. The dissipation of internal tides is significantly enhanced in the upper water column within strongly baroclinic (anticyclonic) eddies, exhibiting a spatially asymmetric pattern, due to trapped high-mode internal tides. Where the eddy velocity opposes the internal tide propagation velocity, high-mode waves can be trapped within the eddy, whereas high modes can freely propagate away from regions where eddy and internal wave velocities are in the same direction. The trapped high modes with large vertical shear are then dissipated, with the asymmetric distribution of trapping leading to the asymmetric distribution of dissipation. Three-dimensional ray tracing solutions further illustrate the importance of the baroclinic current for wave trapping. Similar enhancement of dissipation is also found for a baroclinic cyclonic eddy. However, a barotropic eddy is incapable of facilitating robust high modes and thus cannot generate significant dissipation of internal tides, despite its strong velocities. Both energy transfer from low to high modes in the baroclinic eddy structure and trapping of those high modes by the eddy velocity field are therefore necessary to produce internal wave dissipation, a conclusion confirmed by examining the sensitivity of the internal tide dissipation to eddy radius, vorticity, and vertical scale.

SIGNIFICANCE STATEMENT: The oceanic tides drive underwater waves at the tidal frequency known as internal tides. When these waves break, or dissipate, they can lead to mixing of oceanic heat and salt which impacts the ocean circulation and climate. Accurate climate predictions require computer models that correctly represent the distribution of this mixing. Here we explore how an oceanic eddy, a swirling vortex of order 100–400 km across, can locally enhance the dissipation of oceanic internal tides. We find that strong ocean eddies can be hotspots for internal tide dissipation, for both clockwise and anticlockwise rotating vortices, and surface-enhanced eddies are most effective at internal tide dissipation. These results can improve climate model representations of tidally driven mixing, leading to more credible future predictions.

KEYWORDS: Ocean; Internal waves; Mixing

1. Introduction

Internal waves at the tidal frequency, or internal tides, are widespread in the global ocean where barotropic tides force the oscillation of stratified water at rough topography. Internal tide-induced mixing is estimated to account for approximately half of the energy (~1 TW) sustaining the global overturning circulation (Munk and Wunsch 1998; Egbert and Ray 2000). The horizontal scale of internal tides can range from several kilometers to hundreds of kilometers (Merrifield et al. 2001; Klymak et al. 2011; Zhao and Alford 2009). At present, most climate models do not simulate internal tides, since they do not include astronomical tide forcing, or have the necessary spatial and temporal resolution (Melet et al. 2013). To correctly parameterize internal tidal mixing is therefore an essential task for improving climate models (St. Laurent et al. 2002; Koch-Larrouy et al. 2007; Melet et al. 2016; MacKinnon et al. 2017; de Lavergne et al. 2020). An important step toward an accurate parameterization is to identify where and how the internal tide energy is lost to dissipation and mixing.

Within an ocean bounded by the sea surface above and the seafloor below, the internal tide can be projected onto different vertical normal modes (Gill 1982; Smith and Young 2002; Nycander 2005). Each of these normal modes can then be examined independently and the total behavior of internal tides can be derived by adding the contributions of each mode (Cushman-Roisin and Beckers 2011; Kelly et al. 2012). When barotropic tidal energy is converted to internal tides at the internal tide generation site, a portion of that energy conversion, dependent on the topography and barotropic flow, is in the form of high modes with shorter wavelengths and large shears (Falahat et al. 2014; Wang et al. 2018; Vic et al. 2019). These high modes tend to dissipate in the vicinity of the generation site (Martini et al. 2011; Buijsman et al. 2014). More than half of the internal tide energy is contained in the low modes that can propagate basin-scale distances in the open ocean (Simmons et al. 2004; Arbic et al. 2012; Zhao et al. 2010; Zaron 2019; Buijsman et al. 2020). Therefore, recent research efforts have focused on determining the spatiotemporal redistribution and dissipation of the remotely propagating low-mode internal tides (Melet et al. 2016; Alford et al. 2019; Wang et al. 2021).

Several processes may contribute to the dissipation of low-mode internal tides. The interaction of low modes with topography has received much attention over the past two decades

Corresponding author: Yang Wang, yangwangow@gmail.com

DOI: 10.1175/JPO-D-23-0045.1

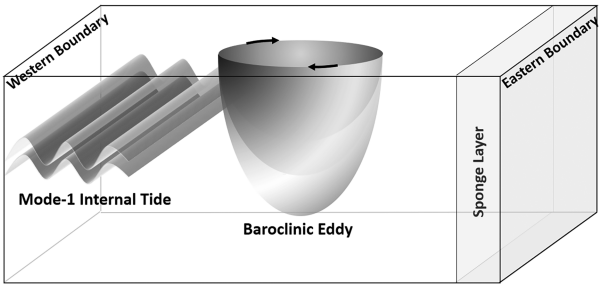

FIG. 1. Schematic showing the model setup for mode-1 internal tide propagating through mesoscale baroclinic eddies.

(Nash et al. 2004; Peacock et al. 2009; Klymak et al. 2016). Small-amplitude topographic features in the open ocean, such as seamounts and small ridges, tend to facilitate the conversion of low-mode energy to higher modes (Johnston et al. 2003; Bühler and Holmes-Cerfon 2011; Mathur et al. 2014). In the presence of large-amplitude ridges, low-mode internal tides have been found to break directly when shoaling topography increases the Froude number above a critical value (Legg 2014). Reflection from topographic slopes at the critical angle and focusing within continental slope canyons also lead to internal wave breaking (Legg and Adcroft 2003; Nazarian and Legg 2017; Alberty et al. 2017). A second pathway for internal tide energy to dissipation is via wave–wave interaction. Weakly nonlinear interactions known as parametric subharmonic instability (PSI), can transfer energy to subharmonic frequencies and higher wavenumbers near the critical latitude (Hibiya et al. 2002; Nikurashin and Legg 2011; MacKinnon 2013; Sun and Pinkel 2013; Ansong et al. 2018; Olbers et al. 2020). Higher harmonics can also be effectively generated in boundary reflection regions where nonlinear processes are enhanced (Tabaei et al. 2005; Peacock et al. 2009).

The possible role of mesoscale eddies as energy sinks for low-mode internal tides is not yet well understood, although previous studies devoted to internal wave–eddy interactions indicate many relevant processes. The dispersion relation for near inertial internal waves in baroclinic background flow has been derived and widely used to explain the propagation characteristics of near-inertial waves (Kunze 1985; Olbers 1981; Jones 2005). When the background flow is dominated by strain rather than vorticity, the wavenumber may increase exponentially, favoring the occurrence of wave capture (Bühler and McIntyre 2005; Polzin 2010; Jing et al. 2018). In terms of internal tides, mesoscale eddies are capable of causing internal tides to be incoherent (dephased from the barotropic tide) (Ponte and Klein 2015; Buijsman et al. 2017; Savage et al. 2020).

Both barotropic and baroclinic mesoscale currents have been found to influence the propagation path of low-mode internal tides (Rainville and Pinkel 2006; Chavanne et al. 2010; Dunphy and Lamb 2014). The varying mesoscale background fields result in spatial gradients of phase and group speed, which cause refraction of the internal tide (Rainville and Pinkel 2006; Zaron and Egbert 2014; Duda et al. 2018; Huang et al. 2018; Wang et al. 2021). Energy transfer from low modes to high modes through internal tide–eddy interaction has been observed in 3D simulations by Dunphy and Lamb (2014). They suggested that high modes are generated when the low modes and eddy satisfy a triad wave–wave–vortex condition as described in Lelong and Riley (1991). Elevated high-mode signals have recently been observed in both cyclonic and anticyclonic eddies (Löb et al. 2020). The subsequent behavior and energy pathways of these high modes need to be explored.

The focus of the present study is the dissipation of low-mode internal tides in mesoscale baroclinic eddies, which has rarely been documented before. We examine the energy propagation paths and corresponding dissipation patterns of internal tides when they pass through eddies with varying spatial scales and magnitudes. A series of high-resolution numerical simulations and theoretical ray-tracing analyses are conducted to address this problem. We find that strong baroclinic eddies (in terms of vorticity magnitude) are capable of trapping the energy transferred to high modes from the mode-1 internal tide, producing enhanced internal tide dissipation in the eddies.

TABLE 1. Parameter settings for the numerical experiments conducted in the present study. The reference case (A150) is indicated in bold font. In experiments beginning with the letter "A" (anticyclonic), the number in the experiment name indicates the eddy radius. For experiments beginning with the letter "V," the number indicates the eddy (anticyclonic) vorticity peak magnitude. With experiments beginning with the letter "H," the number indicates the eddy vertical scale. C150, B150, E150, and T150 indicate the experiments for cyclonic eddy, barotropic eddy, eddy only, and internal tide only, respectively, all with 150-km radius. All eddies except for C150 are anticyclonic.

Expt	Eddy radius (km)	Max horizontal velocity (m s^{-1})	Max vorticity	Vertical scale (m)
A175	175	1.4	-3.0×10^{-5}	1000
A150	**150**	**1.2**	$\mathbf{-3.0 \times 10^{-5}}$	**1000**
A125	125	1.0	-3.0×10^{-5}	1000
A100	100	0.8	-3.0×10^{-5}	1000
A075	75	0.6	-3.0×10^{-5}	1000
V001	150	0.4	-1.0×10^{-5}	1000
V002	150	0.8	-2.0×10^{-5}	1000
H750	150	1.2	-3.0×10^{-5}	750
H500	150	1.2	-3.0×10^{-5}	500
C150 (cyclonic eddy)	150	1.2	3.0×10^{-5}	1000
B150 (barotropic)	150	1.2	-3.0×10^{-5}	1000
E150 (eddy only)	150	1.2	-3.0×10^{-5}	1000
T150 (internal tide only)	—	—	—	—

2. Methodology

a. Model setup

The Massachusetts Institute of Technology General Circulation Model (MITgcm; Marshall et al. 1997) is used to investigate how a baroclinic eddy impacts the energetics of internal tides, using the setup shown in Fig. 1. The three-dimensional simulations are conducted in hydrostatic, implicit free-surface configurations, assuming a linear equation of state for potential density, and an f-plane approximation with $f = 9.3 \times 10^{-5}$ in all simulations, corresponding to midlatitudes in the Northern Hemisphere. Although we use no β effect, so there is no physical north–south direction, for convenience we will label the four horizontal directions north, east, south, and west, as shown in Fig. 1. The model is first initialized with the eddy fields alone, which are allowed to reach a quasi-steady state (adjusting to the boundary conditions and finite domain size). Next, the mode-1 internal tide is forced at the western boundary (Fig. 1). The phase speed of the mode-1 internal tide is about ~2.3 m s^{-1}, with a corresponding horizontal wavelength of about 102 km. The mode-1 internal tide takes about 10 days to propagate through the model domain. We apply a free-slip boundary condition at the bottom, since our goal is to focus on dissipation in the eddy, not the bottom boundary layer. Periodic boundary conditions are used at both northern and southern boundaries. A sponge layer is applied at the eastern boundary to avoid wave reflection. The domain size is 1280 km (east and west boundaries) × 1920 km (south and north boundaries) × 1 km (vertical) with 2000-m horizontal and 20-m vertical resolution. The vertical Laplacian viscosity (A_v) and diffusivity (K_v) have constant values of 10^{-4} m^2 s^{-1}. The horizontal Laplacian viscosity (A_h) and diffusivity (K_h) are set to 10^{-1} m^2 s^{-1}. In the appendix we show that the chosen values of viscosity are small enough that simulated dissipation is not sensitive to decreases in viscosity, while large enough to limit gridscale noise and numerical diffusion. The third-order direct space time (DST) flux limiter advection scheme is used for tracer equations. The time step is set to 15 s, with hourly output in order to adequately extract the internal tide signal.

b. Initialization of the mode-1 internal tide

In the present study, we consider the mode-1 M_2 internal tide passing through baroclinic eddies: in the open ocean, the mode-1 internal tide is the dominant modal component of internal tides. The mode-1 M_2 internal tide is forced at the western boundary following the work of Legg and Adcroft (2003) and Hall et al. (2013), with a frequency of ω. The mode-1 structures for velocity and temperature perturbations are given by

$$u(0, z, t) = U_0 A(z)\sin(\omega t), \tag{1}$$

$$w(0, z, t) = U_0\left[\frac{\omega^2 - f^2}{N^2(z) - \omega^2}\right]^{1/2} B(z)\cos(\omega t), \tag{2}$$

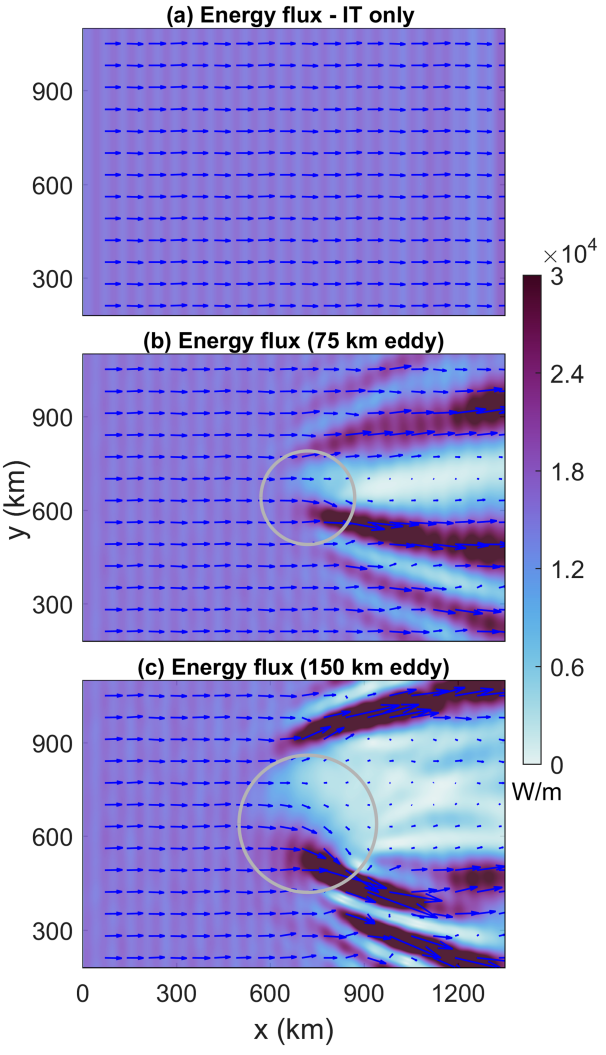

FIG. 2. Depth-integrated and time-averaged baroclinic energy flux of internal tide. (a) Internal tide-only, T150 case, (b) 75-km eddy, A075 case, and (c) 150-km eddy, A150 case. Colors indicate the magnitude and arrows indicate the direction. The gray circles indicate the eddy area with horizontal speed ≥ 0.1 m s^{-1}.

$$T(0, z, t) = T_0(z) - U_0\frac{N(z)}{g\alpha}B(z)\sin(\omega t), \tag{3}$$

where u, w, and T represent the vertical profile of forced horizontal velocity, vertical velocity, and potential temperature, respectively; z is the vertical coordinate; and t is time. The term N is the buoyancy frequency defined as $N = \sqrt{-(g/\rho_0)(\partial\rho/\partial z)}$, which has a constant value of 5.9×10^{-3} rad s^{-1} for the background field. The term ρ is the potential density, ρ_0 is the reference density, and g is the gravitational acceleration. The term α is the thermal expansion coefficient, which is approximated to be constant with a value of 2×10^{-4} K^{-1}. Taking a constant salinity value of 35 psu as a further assumption, the equation of state is linear in our simulation: $\rho = \rho_0(1 - \alpha T)$. The

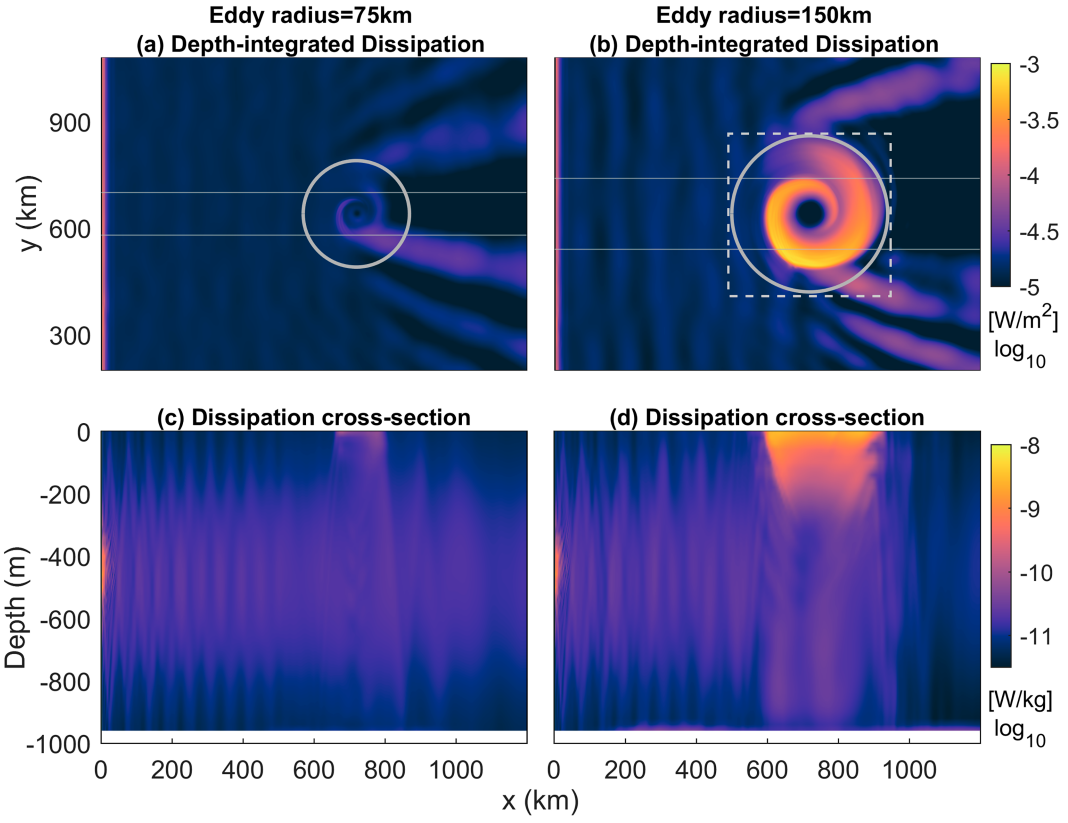

FIG. 3. (a) Depth-integrated and time-averaged tidal dissipation of the 75-km eddy case (A075 case). (b) As in (a), but for the 150-km eddy case (A150 case). (c) Cross section of meridionally averaged (between $y = 540$ km and $y = 740$ km) dissipation rate of the 75-km eddy case. (d) As in (c), but for the 150-km eddy case (meridionally averaged between $y = 450$ km and $y = 830$ km). Colors indicate the magnitude plotted in log scale. The gray lines in (a) and (b) indicate the location for plotting the velocity cross sections in Fig. 6. The gray circles indicate the eddy area with horizontal speed ≥ 0.1 m s^{-1}.

background temperature profile $T_0(z)$ is linear with respect to depth and can be expressed as

$$T_0(z) = \frac{N^2}{g\alpha}(H + z) + T_0(-H). \tag{4}$$

This linear background temperature profile, providing constant background stratification, simplifies the analysis in this idealized scenario.

The term $U_0 = 0.2$ m s^{-1} is the amplitude of the forced mode-1 M_2 internal tide, which is consistent with observational values in areas with strong internal tides. The term H is the water depth, which is 1000 m. The term $B(z)$ is the mode-1 structure for the vertical velocity found by numerically solving the eigenvalue problem

$$B'' + m^2\frac{N(z)^2 - \omega^2}{\omega^2 - f^2}B = 0, \tag{5}$$

in which m is the vertical wavenumber. The term $A(z)$ is the mode-1 structure of horizontal velocity, which can be obtained by taking the vertical derivative of $B(z)$.

c. *Initialization of baroclinic eddy*

An isolated mesoscale eddy is initialized in the central western part of the domain (Fig. 1). The eddy center is located at ($x = 720$ km, $y = 640$ km) where x is the horizontal coordinate in the east–west direction, and y is the horizontal coordinate in the north–south direction, and the origin is in the southwest corner. The sea surface height anomaly (SSHA) follows a Gaussian shape (Zhang et al. 2014)

$$\eta = \left(1 - \frac{r^2}{2L^2}\right)\exp\left(-\frac{r^2}{2L^2}\right), \tag{6}$$

where r is the distance from the eddy center and L is the radius of the eddy.

Then the surface horizontal geostrophic current can be obtained

$$u_{g0} = -\frac{g}{f}\frac{\partial\eta}{\partial y}, \tag{7}$$

$$v_{g0} = \frac{g}{f}\frac{\partial\eta}{\partial x}. \tag{8}$$

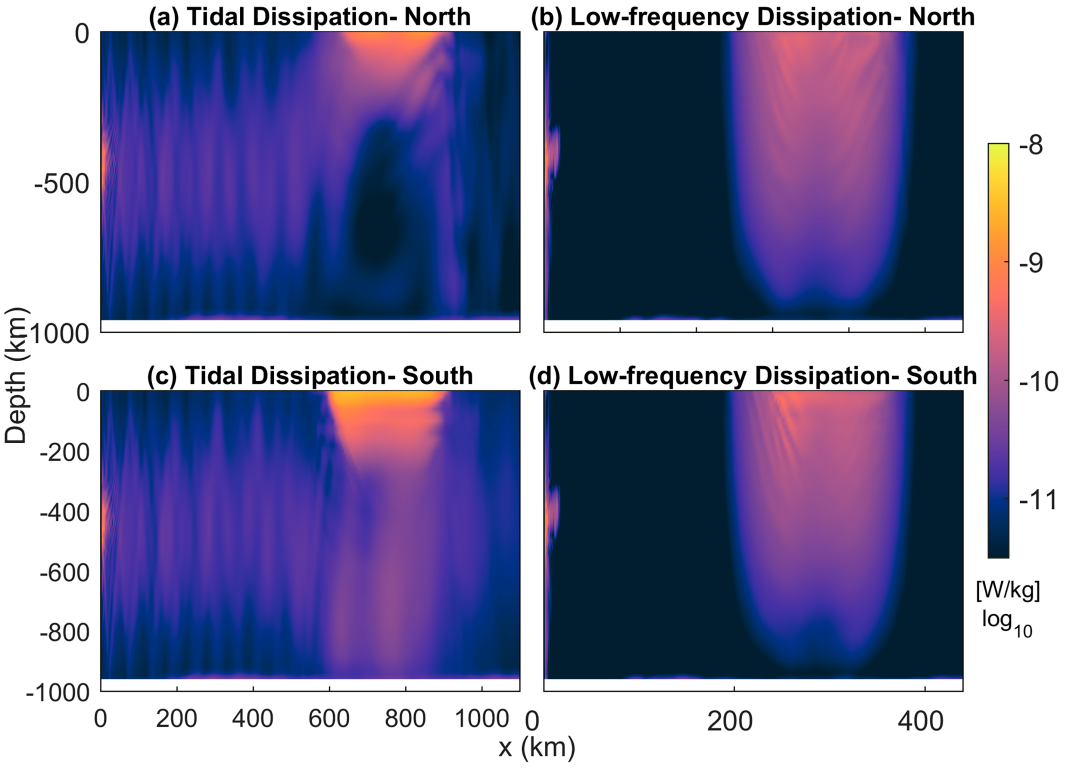

FIG. 4. Cross sections for time-averaged dissipation in the reference case (A150 case). (a) Cross section of meridionally averaged (between $y = 640$ km and $y = 830$ km) tidal dissipation rate in northern sector. (b) Cross section of meridionally averaged (between $y = 640$ km and $y = 830$ km) low-frequency dissipation rate in northern sector. (c) As in (a), but for the southern sector (between $y = 450$ km and $y = 640$ km). (d) As in (b), but for the southern sector. Colors indicate the magnitude in log10 scale.

The vertical structure of horizontal velocity and perturbation pressure is specified as a half sine shape (Zhang et al. 2014) with water depth H, so that the eddy anomaly vanishes at the seafloor (for some later experiments, eddies with smaller vertical scales are used, with the same shape, but anomalies which vanish at a height above the seafloor and remain zero down to the bottom):

$$u_g(z) = u_{g0}\left[1 + \sin\left(\frac{\pi z}{2H}\right)\right], \tag{9}$$

$$p'(z) = P_0\left[1 + \sin\left(\frac{\pi z}{2H}\right)\right] = \rho_0 g\eta\left[1 + \sin\left(\frac{\pi z}{2H}\right)\right]. \tag{10}$$

Since our study considers eddies that have different intensities (as characterized by the peak vorticity), in some experiments (Table 1), the Rossby number can reach values as high as $O(10^{-1})$. The centrifugal force resulting from the rotational speed is nonnegligible in these cases. Therefore, the centrifugal force is incorporated (Douglass and Richman 2015),

$$u_{\rm gr} = \frac{g}{f}\frac{\partial\eta}{\partial r} + \frac{u_{\rm gr}^2}{fr}. \tag{11}$$

The gradient rotational speed $u_{\rm gr}$ can be obtained by solving this quadratic equation. The solution reads (Knox and Ohmann 2006),

$$u_{\rm gr} = \frac{2u_g(r)}{1 \pm \sqrt{1 + 4u_g(r)/fr}}. \tag{12}$$

With hydrostatic balance, we can determine the density anomaly

$$\rho'(z) = -\frac{1}{g}\frac{\partial p'}{\partial z} = -\frac{\pi}{2H}\rho_0\eta\cos\left(\frac{\pi z}{2H}\right). \tag{13}$$

The temperature perturbation caused by the mesoscale eddy can be derived using the linear equation of state.

To investigate the sensitivity of internal tide energy to the magnitude and size of eddies, a series of numerical experiments are performed (Table 1). Both the horizontal and vertical scales of eddies are varied separately in the simulations. The main body of the analysis is focused on the baroclinic anticyclonic eddy cases. A barotropic eddy case and a baroclinic cyclonic eddy case are also conducted for comparison. The 150-km radius baroclinic anticyclonic eddy experiment is used as the reference case. An internal tide-only experiment and

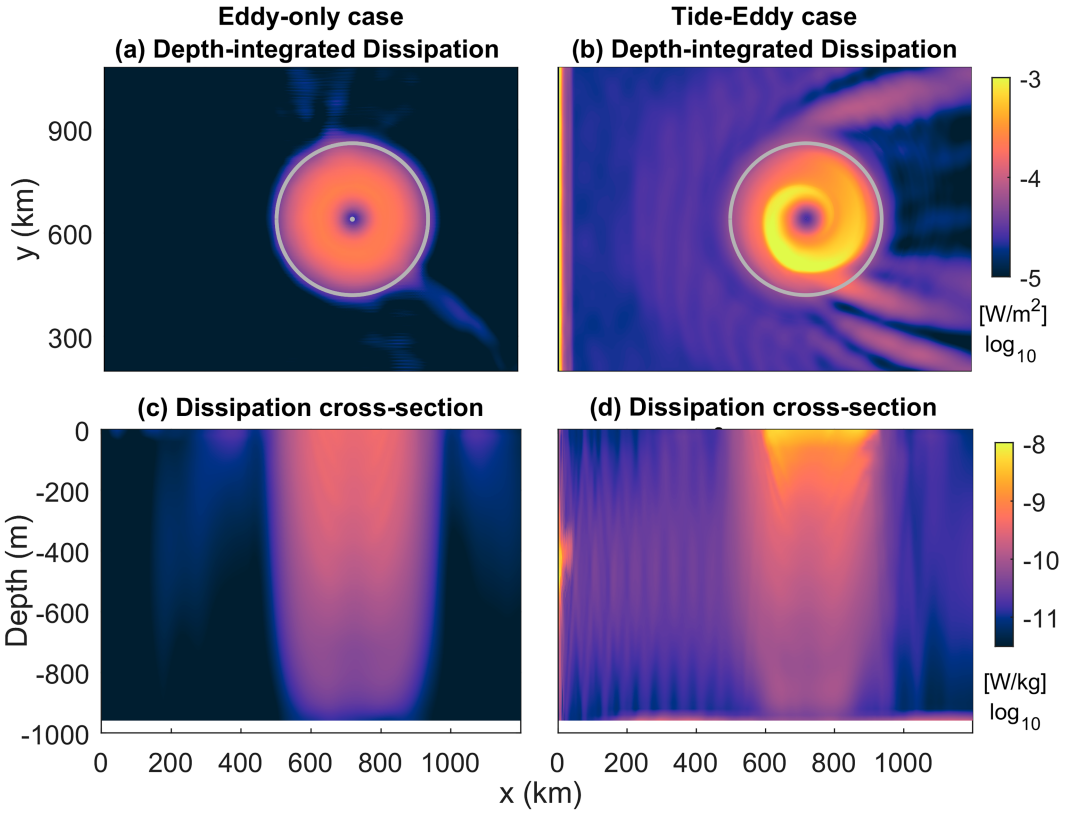

FIG. 5. (a) Depth-integrated and time-averaged (averaging over two inertial cycles) dissipation of the eddy-only experiment (E150). (b) Depth-integrated and time-averaged dissipation for all frequencies (full dissipation) of the reference case (A150). (c) Cross section of meridionally averaged (between $y = 450$ km and $y = 830$ km) dissipation rate of the eddy-only experiment (E150) (eddy-induced dissipation). (d) As in (c), but for the reference case. Colors indicate the magnitude plotted in log10 scale. The gray circles in (a) and (b) indicate the eddy area with horizontal speed ≥ 0.1 m s^{-1}.

an eddy-only experiment (150-km radius) are performed for comparison.

d. *Energy equation and vertical modes*

The baroclinic energy flux of the internal tide is calculated to diagnose the energy propagation, which is given by (Nash et al. 2006; Niwa and Hibiya 2004; Kang and Fringer 2012)

$$\overline{F} = \overline{\int_{-H}^{0} u'p'\,dz}\,, \tag{14}$$

where the overbar denotes a time average over two tidal cycles (we have also verified that averaging over six tidal cycles closely approximates the results over two tidal cycles). The term u' is the horizontal velocity at tidal frequency. The (hydrostatic) perturbation pressure p' is defined as

$$p' = p_{\text{surf}} + g\int_{z}^{0} \rho'\,dz'\,, \tag{15}$$

in which ρ' is the tidal-frequency perturbation density relative to the period-averaged condition and p_{surf} can be inferred by applying the baroclinic condition that

$$\frac{1}{H}\int_{-H}^{0} p'\,dz = 0. \tag{16}$$

The dissipation rate is calculated as

$$\epsilon = A_v\overline{\left(\frac{\partial \mathbf{u}}{\partial z}\right)^2} + A_H\left[\overline{\left(\frac{\partial \mathbf{u}}{\partial x}\right)^2} + \overline{\left(\frac{\partial \mathbf{u}}{\partial y}\right)^2}\right]. \tag{17}$$

The present resolutions allow us to resolve the eddy motions and high-wavenumber internal waves. However, instability and wave breaking cannot be directly resolved. Dissipation of internal tides in the open ocean is strongly related to the shear-driven instability (Polzin et al. 1995; Thorpe 2018). In the present model configuration, the model Laplacian viscosity is responsible for explicit dissipation, which is diagnosed according to Eq. (17), and which concentrates dissipation in regions of resolved shear. This scheme has been widely used for evaluating dissipation of internal tides by model-based studies (Buijsman et al. 2012; Nagai and Hibiya 2015). The diagnosed dissipation using this scheme is consistent with the modeled high-wavenumber and high-shear structure of internal tides. Numerical simulations also

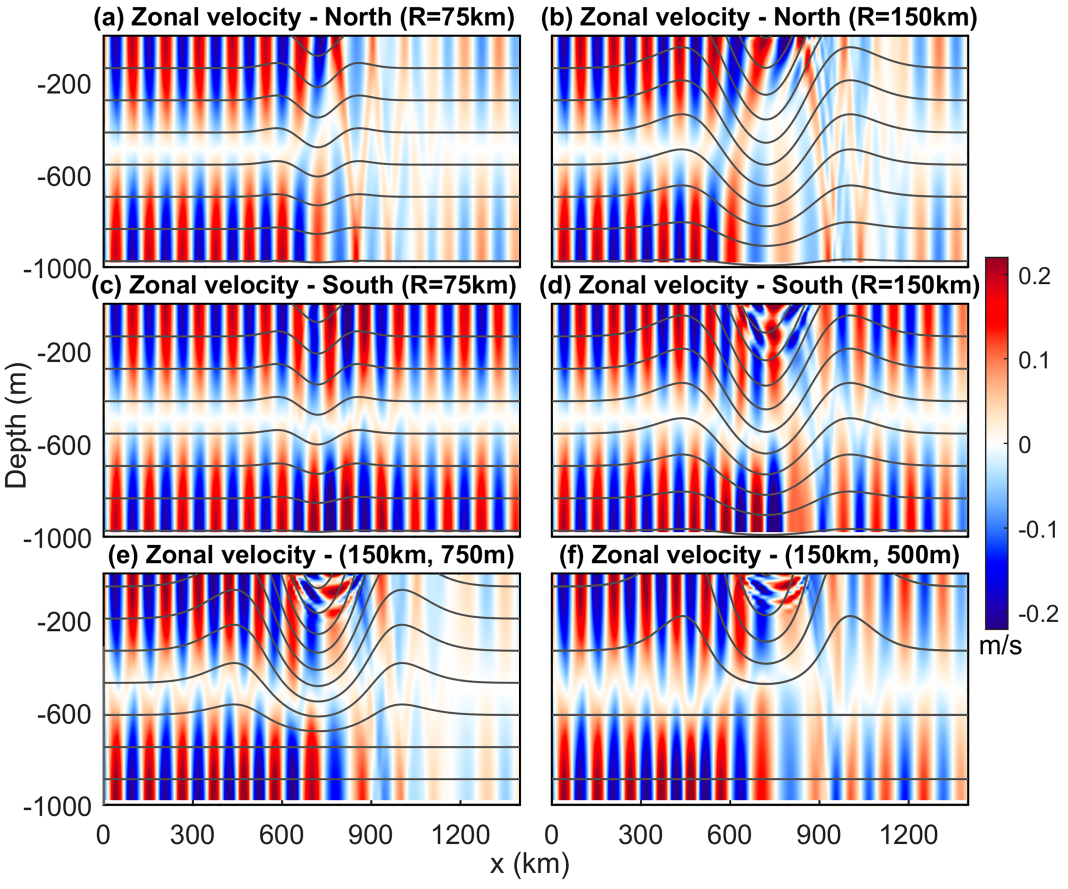

FIG. 6. Transects (the locations of the transects are indicated by the gray lines in Figs. 3a,b) of instantaneous baroclinic tidal zonal velocity at day 11 of the simulation. (a) Northern and (c) southern sector of the 75-km anticyclonic eddy (A075 case). (b),(d) As in (a) and (c), but for the 150-km anticyclonic eddy (A150 case). (e),(f) As in (d), but for the 150-km anticyclonic eddies with vertical scale of 750 m (H750 case) and 500 m (H500 case), respectively. Colors indicate the magnitude. The black lines in each panel indicate the time-mean isopycnals for each case.

often include implicit numerical dissipation, which cannot be directly diagnosed. In our simulations, the diagnosed dissipation agrees well with the divergence of the internal tide energy flux (not shown), indicating that the explicitly diagnosed dissipation appropriately captures the internal tide energy loss in the present study.

Since the tidal-frequency energy can be transferred to higher harmonics prior to dissipation, when calculating the internal tide dissipation, $\mathbf{u}$ represents the high-pass (cutoff frequency: $0.9\omega_{m2}$) filtered horizontal velocity. For the low-frequency dissipation $\mathbf{u}$ represents the low-pass [cutoff frequency: $(1/3)f$] filtered horizontal velocity. The raw (unfiltered) horizontal velocity is used for calculating the full dissipation over all frequencies in the internal tide–eddy cases and the dissipation in the eddy-only experiment (eddy-induced dissipation).

The vertical structure of internal tides can be projected onto a linear combination of dynamical modes (Kelly et al. 2012; Buijsman et al. 2014)

$$\mathbf{u}(x, y, z) = \sum_{n=0}^{\infty} \mathbf{u}_n(x, y)\phi_n(x, y, z), \tag{18}$$

$$p(x, y, z) = \sum_{n=0}^{\infty} p_n(x, y)\phi_n(x, y, z), \tag{19}$$

where ϕ_n is the vertical structure function of horizontal velocity and perturbation pressure. The terms $\mathbf{u}$ and p are fitted to a discrete set of $\mathbf{u}_n$ and p_n using a least squares regression.

The energy equation for a specific mode n assuming a linear and inviscid system is (Kelly et al. 2016)

$$\frac{\partial}{\partial t}\left(\frac{H}{2}|\mathbf{u}_n|^2 + \frac{H}{2}\frac{p_n^2}{c_n^2}\right) + \nabla\cdot(\mathbf{u}_n p_n) = \sum_{m=0}^{\infty} C_{mn}, \tag{20}$$

where the first term is the energy tendency and the second term is the energy flux divergence. The c_n represents eigenspeed for mode n. Note that the dissipation term resulting from finite viscosity and the nonlinear advection term are omitted in the derivation of Eq. (20). Our goal here is to primarily focus on the energy transfer term C_{mn} in Eq. (21), which represents energy conversion from mode m to mode n:

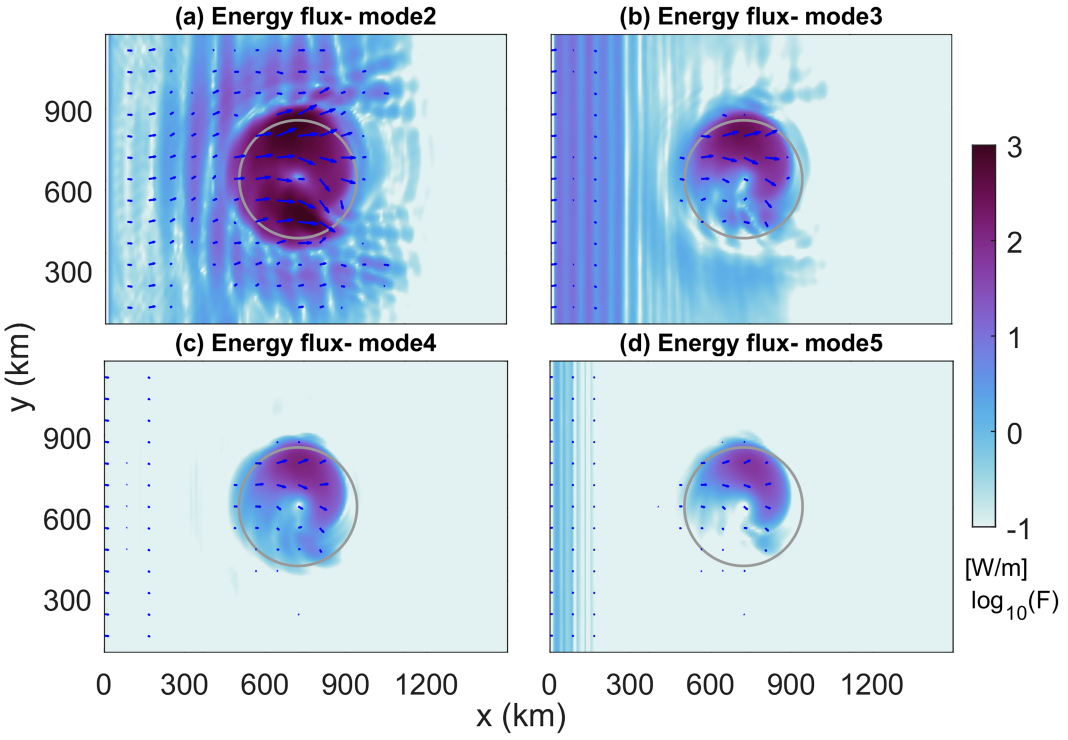

FIG. 7. Horizontal distribution of depth-integrated and time-averaged baroclinic tidal energy flux ($\overline{F}_n = \overline{\int_{-H}^{0} u_n' p_n' \, dz}$ where n is the mode number) for (a) mode 2, (b) mode 3, (c) mode 4, and (d) mode 5 around day 7 of the reference case (A150). Colors indicate the magnitude of energy flux. Arrows indicate both the direction and magnitude. The gray circles indicate the eddy area with horizontal speed ≥ 0.1 m s^{-1}.

$$C_{mn} = \int_{-H}^{0} \mathbf{u}_m \cdot \nabla p_n - \mathbf{u}_n \cdot \nabla p_m \, dz \,. \tag{21}$$

This conversion term is calculated to quantify the energy transfer from the incident mode-1 internal tides to higher modes, as well as identify the locations of the energy transfer.

e. *Ray tracing of internal tide energy*

Each vertical mode is a standing wave in the vertical, consisting of superposed upward and downward propagating waves, which each satisfies the internal wave dispersion relation (Smith and Young 2002). The wave energy therefore radiates in the form of upward and downward propagating energy rays. The energy ray-tracing method is utilized to theoretically investigate the three-dimensional path of these energy rays. The wavenumber and group velocity of the internal tide will be altered by the baroclinic eddy field. As a result, the internal tide will be refracted, changing its propagation path (Olbers 1981; Chavanne et al. 2010). In this approach, we make the WKB approximation, assuming that the properties of the medium through which the wave is traveling, such as the stratification and fluid velocity, change over length scales that are large compared to the wavelength of the wave (Jones 1969; Olbers 1981). This contrasts with the modal approach where the vertical structure of the mode may correspond to a wavelength that is large relative to the depth of the fluid. Nonetheless, by separating each vertical mode into an upward and downward propagating wave pair, the ray-tracing method can reveal useful qualitative information about the wave energy path, despite being applied in a regime where the WKB assumption is not strictly valid (Kunze 1985; Chavanne et al. 2010).

The ray trajectory of internal tide energy is governed by the propagation equation

$$\omega = \omega_0 + \mathbf{k} \cdot \mathbf{U} \,, \tag{22}$$

$$\frac{d\mathbf{x}}{dt} = \mathbf{C}_g = \frac{\partial \omega}{\partial \mathbf{k}} = \mathbf{C}_{g0} + \mathbf{U} \,, \tag{23}$$

where ω_0 is the intrinsic frequency, $\mathbf{C}_g$ is the group velocity, $\mathbf{U}$ is the background baroclinic velocity, and $\mathbf{k}(k, l, m)$ is the wavenumber vector, where k, l, and m are the wavenumbers in the x, y, and z directions, respectively. The intrinsic group velocity is derived from the dispersion relation

$$\omega_0^2 = f^2 + N^2 \frac{k^2 + l^2}{m^2} \,, \tag{24}$$

$$\mathbf{C}_{g0} = \frac{\partial \omega_0}{\partial \mathbf{k}} = \left(\frac{N^2 k}{\omega_0 m^2}, \frac{N^2 l}{\omega_0 m^2}, -\frac{\omega_0^2 - f^2}{\omega_0 m} \right). \tag{25}$$

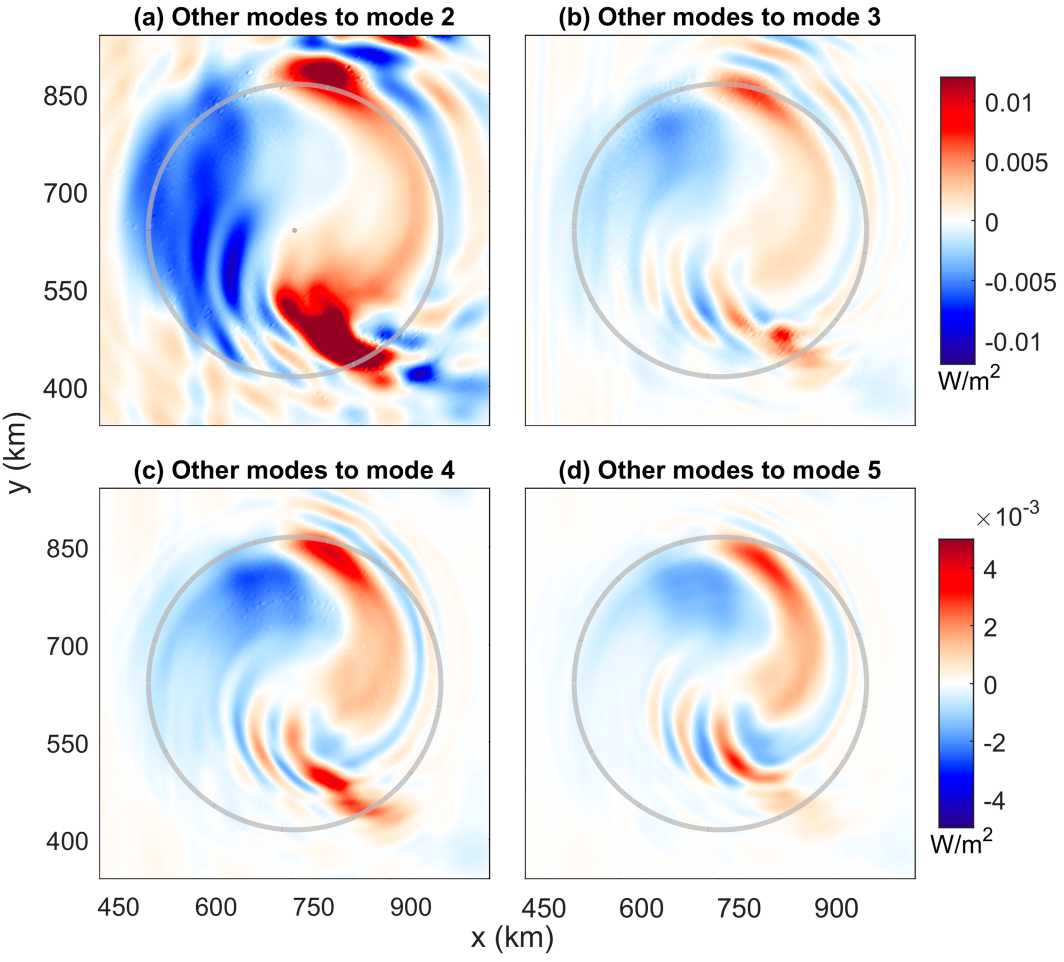

FIG. 8. Depth-integrated and time-averaged energy transfer between different modes of the reference case (A150). (a) Energy transferred to mode 2 from other modes. (b)–(d) As in (a), but for modes 3–5. Colors indicate the magnitude. The gray circles indicate the eddy area with horizontal speed ≥ 0.1 m s^{-1}.

The wavenumber is modulated by the refraction equation

$$\frac{d\mathbf{k}}{dt} = \mathbf{r} = -\frac{\partial \omega}{\partial \mathbf{x}} = \mathbf{r}_0 - k\frac{\partial U}{\partial \mathbf{x}} - l\frac{\partial V}{\partial \mathbf{x}} - m\frac{\partial W}{\partial \mathbf{x}}, \tag{26}$$

$$\mathbf{r}_0 = -\frac{\partial \omega_0}{\partial \mathbf{x}} = -\frac{\omega_0^2 - f^2}{\omega_0 N}\frac{\partial N}{\partial \mathbf{x}}, \tag{27}$$

where $\mathbf{r}$ is the refraction rate and $\mathbf{r}_0$ is the intrinsic refraction rate. By numerically integrating Eq. (23), we can find the 3D energy ray path of the internal tide.

3. Results

a. Refracted energy pattern

Overall, we find that a baroclinic eddy can significantly alter the propagation pattern of the mode-1 internal tide. The simulated baroclinic energy flux of three representative experiments is shown in Fig. 2, which comprise the internal tide-only case (T150), 75-km eddy case (A075), and 150-km eddy case (A150), respectively. The incident mode-1 energy flux propagates due east in the internal tide-only case, with no significant decay (Fig. 2a). For the other two cases influenced by eddies, the energy flux exhibits a uniform pattern with magnitude of 15 kW m^{-1} before encountering the eddy field. After interacting with the eddy, by contrast, the energy flux is refracted into beams (Figs. 2b,c). Two beams are seen emanating from the northern and southern sectors of the eddy (hereafter the "northern sector" represents the eddy region north of the central axis, the "southern sector" refers to the opposite area), propagating northeast and southeast, respectively.

This refraction effect is more prominent in the larger eddy case (A150) (Fig. 2c). The refracted beams possess strong energy flux reaching a magnitude of 30 kW m^{-1}. Since the refraction confines the energy flux to localized beams, the internal tide energy in the lee of the eddy is much reduced, e.g., energy flux decreases to <5 kW m^{-1} in the lee area of the eddy.

b. Enhanced dissipation

The depth-integrated and time-averaged tidal dissipation for the 75-km eddy case (A075) and 150-km eddy case (A150)

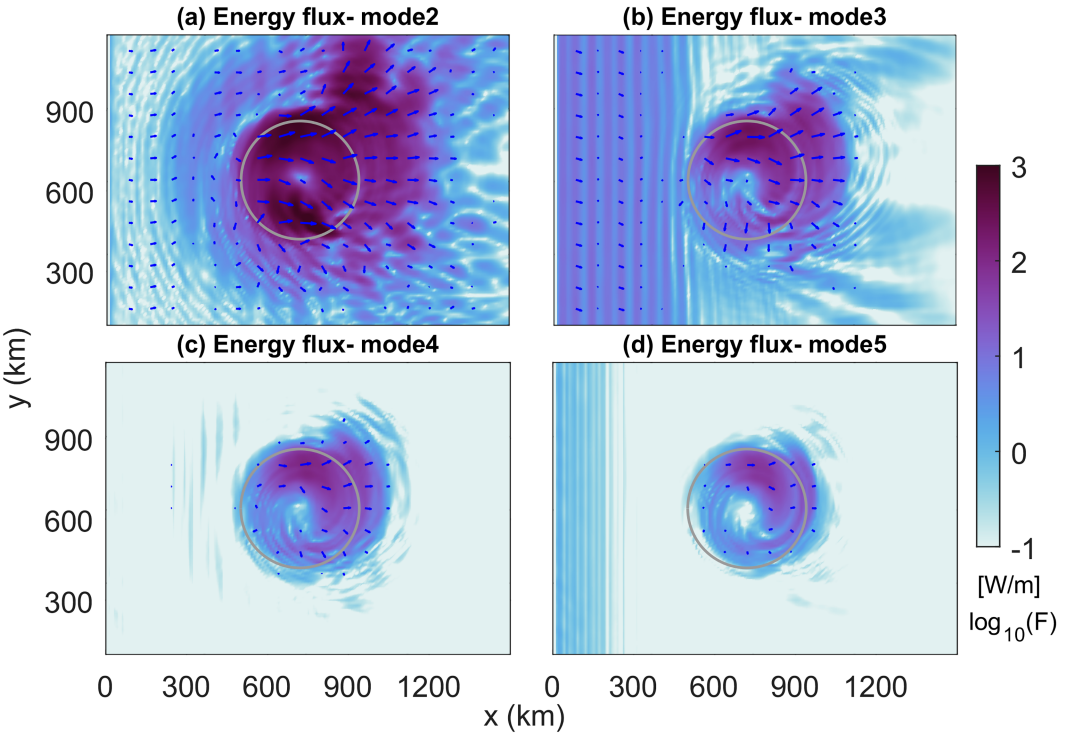

FIG. 9. As in Fig. 7, but for horizontal distribution of depth-integrated and time-averaged baroclinic tidal energy flux around day 14 of the reference case (A150). Colors indicate the magnitude of energy flux density. Arrows indicate both the direction and magnitude. The gray circles indicate the eddy area with horizontal speed ≥ 0.1 m s^{-1}.

are shown in Fig. 3. For the smaller eddy, slightly enhanced dissipation is found along the converged energy flux beams (where energy flux is concentrated and enhanced) (Fig. 3a), where the depth-integrated dissipation rate is several times larger than that in the rest of the model domain. In the case of the larger eddy, however, much more vigorous dissipation occurs in the vicinity of the eddy, with maximum magnitude of $\sim 1 \times 10^{-3}$ W m^{-2} (Fig. 3b). The dissipation exhibits a spiral pattern with north–south asymmetry. Specifically, the dissipation in the southern sector of the eddy (where eddy velocities oppose the internal wave propagation) is much stronger than that in the northern sector (where the eddy velocity is in the same direction as the internal wave propagation). The depth-integrated dissipation rate is an order of magnitude larger than that in the smaller eddy case (Fig. 3b).

We look further into the vertical distribution of the dissipation rate for the two different sized eddy simulations. The cross sections of meridionally averaged dissipation rate for the 75-km eddy and 150-km eddy are presented in Figs. 3c and 3d. Compared to the smaller eddy (Fig. 3c), the dissipation within the eddy region of the larger eddy is enhanced in the vertical section (Fig. 3d). The enhanced patterns are confined to the upper column of the eddy, where the dissipation rate reaches $10^{-8.5}$ W kg^{-1}. The dissipation level outside the eddy region only reaches the order of $10^{-10.5}$ W kg^{-1} (Fig. 3d). Similar to the north–south asymmetry seen in the horizontal plane, the dissipation also extends over a broader area in the vertical in the southern sector of the eddy (Fig. 4c versus Fig. 4a).

The eddy-induced dissipation in the eddy-only experiment (E150) and the full dissipation in the reference internal tide–eddy case (A150) are also calculated for comparison (Fig. 5). The distribution of the dissipation in the eddy-only case is spread symmetrically in the horizontal, with a maximum magnitude of $\sim 3 \times 10^{-4}$ W m^{-2}, which is approximately one-third of the magnitude of the depth-integrated tidal dissipation (Fig. 5a versus Fig. 3b). In the vertical, the eddy-induced dissipation in the eddy-only case extends throughout the water column, spanning the magnitude of $10^{-10.5}$–10^{-9} W kg^{-1} in the eddy region (Fig. 5c). Although our dissipation of this large-scale structure is associated with our large model viscosities, the magnitude of our simulated eddy-induced dissipation is reasonably consistent with some recent observations in areas with strong eddies, such as the Gulf of Mexico (Molodtsov et al. 2020) and the Southern Ocean (Sheen et al. 2014).

The full dissipation in the internal tide–eddy case (A150) is consistent with the compounded pattern of tidal dissipation in the internal tide–eddy case (A150) (Fig. 3b) and eddy-induced dissipation in the eddy-only case (E150) (Figs. 5a). Hence the additional dissipation compared to the eddy-only case is due to the dissipation of the internal tide, and initiated by the interaction of the internal tide with the eddy. The mechanism and processes that lead to this enhanced internal tidal dissipation are investigated in the following subsections.

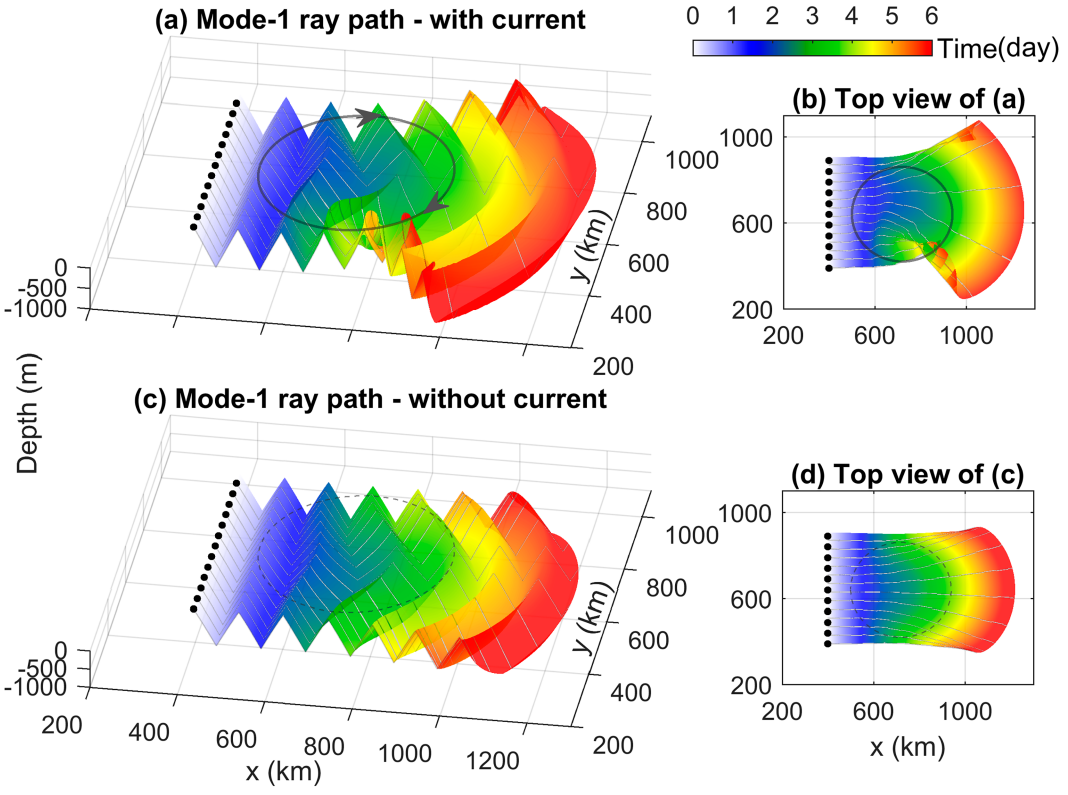

FIG. 10. The 3D ray paths for mode-1 internal tide for the reference case (A150). (a) Computed mode-1 ray paths incorporating both eddy current and stratification. (b) The top view of (a). (c) Computed mode-1 ray paths with only incorporating the stratification. (d) Top view of (c). The colors indicate the 3D ray surface and propagation time. The gray lines indicate the ray paths. The gray circles in (a) and (b) indicate the eddy area with horizontal speed ≥ 0.1 m s^{-1}.

c. *Evolution and contribution of high modes*

The high-mode internal tides have larger vertical wavenumber, accompanied by larger vertical shear, tending to contribute more to the dissipation (Legg 2004; Klymak et al. 2008; Kelly et al. 2012). To explore whether the high modes play an important role in the enhanced dissipation, we first examine whether high modes are generated during the internal tide–eddy interaction. The transects of baroclinic tidal velocity are presented in Fig. 6 to examine the vertical structure of the internal tide. For the smaller eddy case, the zonal tidal velocity is slightly affected to generate a beam-like vertical structure (see middle of Fig. 6a) in the northern sector of the eddy. This effect is less significant in the southern sector of the smaller eddy (Fig. 6c).

Significant high-wavenumber structures can be identified in the larger eddy case (Figs. 6b,d). In the northern sector of the larger eddy, the vertical structure of zonal velocity is noticeably scattered to oblique beam patterns (Fig. 6b). This vertical beam structure is generated by the superposition of different modes, indicating that high modes are produced due to internal tide–eddy interaction. The most intriguing feature is that abundant high-wavenumber signals are found in the upper half of the water column in the southern sector of the larger eddy, but they do not propagate further out of the eddy area (Fig. 6d). This finding indicates that the high modes may be trapped and then contribute to the enhanced dissipation.

We further examine the baroclinic tidal energy flux of high modes at different stages of the reference simulation. Figure 7 shows the depth-integrated and time-averaged energy flux density of modes 2–5 around the simulation time of day 7. At this stage, the high modes have been generated but have not yet propagated eastward out of the eddy region. The mode-2 energy flux density in both northern and southern sectors of the eddy have comparable magnitudes up to 10^3 W m^{-1} (Fig. 7a). The mode-3 and higher modes, however, display relatively larger energy flux density in the northern sector of the eddy than in the southern sector (Figs. 7b–d).

We explore sources of asymmetry in the high mode energy by calculating the energy transfer between different modes (Fig. 8). The energy transfer rate for mode 2 exhibits a pattern that is generally comparable on the north and south sides of the eddy, with a somewhat larger transfer rate in the southern sector (Fig. 8a). This pattern for mode 2 is consistent with the energy flux pattern shown in Fig. 7a. For modes 3–5, the energy transfer rate is relatively larger in the northern sector (Fig. 8), also generally mimicking the distribution of energy flux. The transfer rate has a sizable region of negative values, which indicates the energy of mode n cascading to other modes. Note that the horizontal and vertical structure of

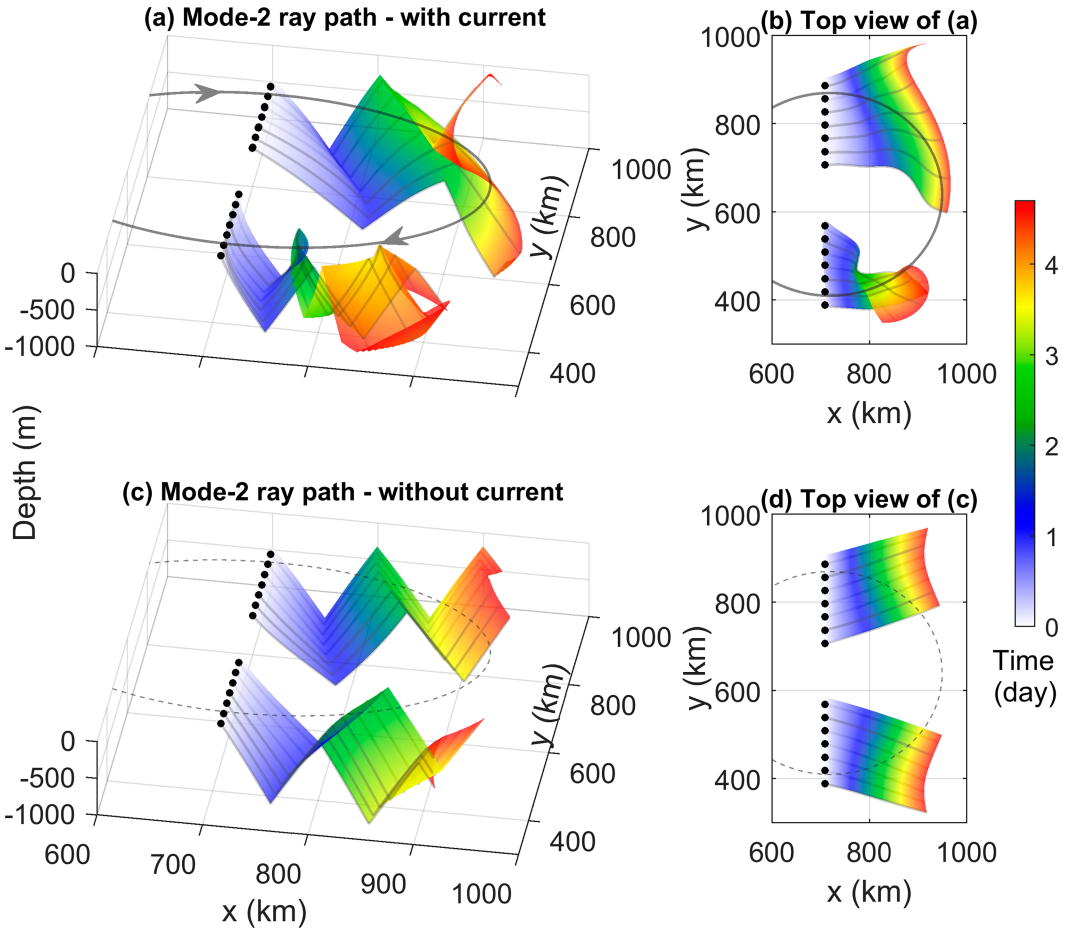

FIG. 11. The 3D ray paths for mode-2 internal tide for the reference case (A150). (a) Computed mode-2 ray paths incorporating both eddy current and stratification. (b) The top view of (a). (c) Computed mode-2 ray paths only incorporating the stratification. (d) Top view of (c). The black dots represent the initial positions of the mode-2 rays. The colors indicate the 3D ray surface and propagation time. The gray lines indicate the ray paths. The gray circles in (a) and (b) indicate the eddy area with horizontal speed ≥ 0.1 m s^{-1}.

stratification in the eddy region are axisymmetric. The north–south asymmetry seen in the energy transfer for modes 3–5 is therefore most likely induced by the contrasting directions of the background eddy currents. The present simulation results find more scattering to higher modes (mode 3 and higher) in regions where the internal tide is propagating in the same direction as the background current. However, since we show later that this scattering to higher modes does not occur in a barotropic eddy, the shear is likely more important than the absolute velocity.

Around day 14, the propagation patterns of high modes present more pronounced north–south asymmetries (Fig. 9). In the northern sector, the high-mode energy radiates further from the eddy and mainly spreads in the northeast direction. For example, the radiation pattern of mode 2 in the northern sector exhibits a broader coverage and a greater magnitude (Fig. 9a). In the southern sector, on the other hand, mode 2 has a smaller radiation range and a weaker magnitude. The asymmetric propagation features suggest that the high-mode energy in the southern sector propagates more slowly and may experience trapping.

d. Ray tracing and trapped high modes

In this section, to better interpret the simulated enhanced dissipation of internal tides, we conduct ray tracing to calculate the three-dimensional energy paths of different modes in the baroclinic eddy. The 3D ray paths are determined as the group velocity and wavenumber are modulated by the spatial-varying background. We apply ray tracing to the 150-km eddy case (reference case A150). For this case, the horizontal wavelength of internal tide (~102, ~51, and ~34 km for mode 1, 2, and 3, respectively) is smaller than the horizontal scale of the 150-km eddy, suggesting some validity of WKB approximation (although this is not true for the vertical length scale of the mode-1 wave which is larger than the depth of the fluid). Initial modes 1, 2, and 3 have horizontal phase speeds of 2.3, 1.15, and 0.75 m s^{-1}, respectively, and horizontal group speeds of 1.4, 0.7, and 0.45 m s^{-1}.

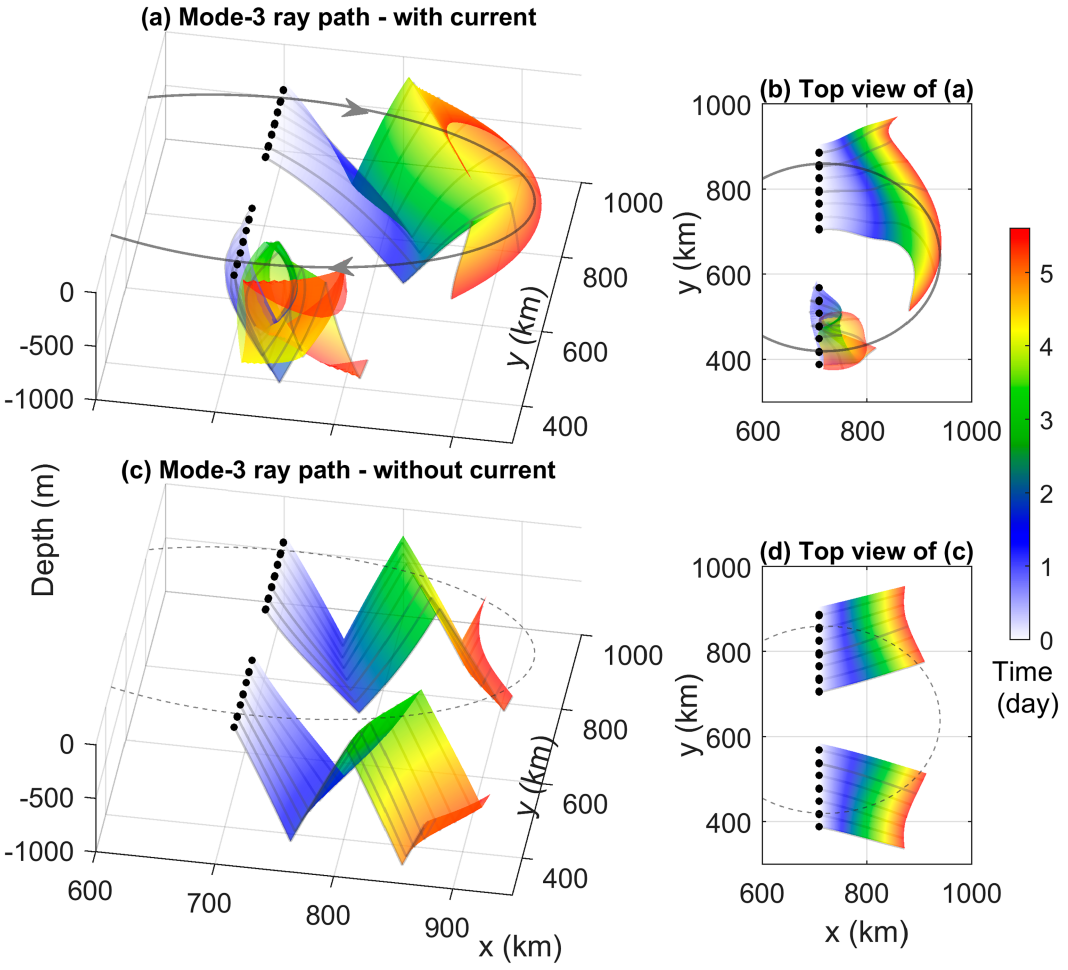

FIG. 12. The 3D ray paths for mode-3 internal tide for the reference case (A150). (a) Computed mode-3 ray paths incorporating both eddy current and stratification. (b) The top view of (a). (c) Computed mode-3 ray paths only incorporating the stratification. (d) Top view of (c). The black dots represent the initial positions of the mode-3 rays. The colors indicate the 3D ray surface and propagation time. The gray lines indicate the ray paths. The gray circles in (a) and (b) indicate the eddy area with horizontal speed ≥ 0.1 m s^{-1}.

Modes are stationary waves in the vertical, which can be considered a superposition of upward-propagating and downward-propagating waves. Here we examine the path of the wave component which is initially propagating downward from the surface. The mode-1 rays with horizontal wavelengths of 102 km are initialized along the $x = 400$ km line and near the surface where the incident mode-1 waves have not hit the eddy region (black dots in Fig. 10a). The horizontally propagating directions for the initial mode-1 waves are set to due east, in accordance with the simulation (Fig. 2c). The initial vertical slope of the ray is determined from the initial group velocity. The vertical slope $S = \sqrt{C_{gz}^2/(C_{gx}^2 + C_{gy}^2)} = \sqrt{(\omega^2 - f^2)/(N^2)}$ depends on wave frequency and environmental parameters and is independent of mode number. As the mode-1 rays encounter the eddy field, the ray surface is noticeably refracted so that ray paths spread outward (Figs. 10a,b). The mode-1 ray paths form two converged beams near the northern and southern edge area of the eddy (Fig. 10b), resembling the simulated energy flux pattern (Fig. 2c). Another intriguing phenomenon is that some of the rays in the southern sector are still trapped in the eddy after 5 days' integration, while all the rays in the northern sector can freely and more rapidly propagate out of the eddy (Fig. 10b).

To distinguish the effect of the baroclinic current from that of the stratification on the ray paths, we then separately compute the ray paths of mode-1 internal waves only incorporating the stratification, ignoring the eddy velocity field. In the mode-1 without-current case, as shown in Figs. 10c and 10d, the 3D ray surface shows a pattern which is symmetric in the north–south direction. The mode-1 rays in both the northern and southern sectors can propagate far away from the eddy region after 6 days' integration. The ray paths are refracted much less than the with-current case (Fig. 10d versus Fig. 10b).

The mode-2 and mode-3 waves are initialized along the $x = 720$ km line and near the surface (black dots in Figs. 11 and 12), where the mode-2 and mode-3 energy are effectively generated (Fig. 7). The initial horizontal directions for the rays are set to 10 degrees north of east in the northern sector and 10 degrees south of east in the southern sector, respectively, to approximate the simulated directions. The initial vertical slopes S of the mode-2 and mode-3 rays are also determined by $S = \sqrt{(\omega^2 - f^2)/(N^2)}$. Different from the mode-1 wave ray tracing, the initial mode-2 and mode-3 waves are located well within the eddy region, since the simulation results indicate this is the generation location.

Both the mode-2 and mode-3 rays in the southern sector of the eddy are substantially trapped as they propagate within the eddy (Figs. 11a and 12a). The mode-2 ray surface in the southern sector is greatly distorted and constrained to a narrow pattern (Fig. 11a). The mode-3 rays in the southern sector are even more twisted and focused locally. (Fig. 12b). All the mode-3 rays in the southern sector are effectively trapped in the eddy. Most of the energy rays of mode 2 and mode 3 in the northern sector can escape from the eddy, while some rays close to the eddy core may also be captured by the eddy and follow a spiral trajectory (Figs. 11b and 12b). For the without-current cases of both mode 2 and mode 3, the energy rays in the two sectors radiate in north–south symmetric patterns (Figs. 11c and 12c).

Our ray-tracing results demonstrate that the high modes in the southern sector of the anticyclonic eddy could experience strong trapping by the eddy velocities. The trapped high-mode energy could therefore be responsible for the enhanced dissipation in the southern sector. It should be noted that the ray tracing here only calculates the energy path but not the loss of energy along that path through dissipation. In the full simulations, the trapped high-mode waves may dissipate more rapidly than our ray-tracing integration time. In contrast, most of the high-mode energy in the northern sector propagates outward or escapes the eddy easily. These differences in ray paths could explain why the dissipation is enhanced in the southern sector of the eddy, despite the greater higher-mode energy flux in the northern sector.

e. *Barotropic eddy case*

To further illustrate the essential role of the baroclinic (BC) eddy structure, a barotropic (BT) eddy experiment is performed. The radius of the barotropic eddy is also 150 km, as for the reference eddy. There are two differences between the barotropic and baroclinic eddy case. First, the barotropic eddy has a depth-invariant velocity field. Second, the barotropic velocity is only balanced by the gradient of sea surface height; the stratification of the barotropic eddy is therefore horizontally uniform. In this case, the impact of the eddy on the mode-1 internal tide only comes from the horizontally varying eddy current field.

The modeled results of the BT case differ from the BC case in both the energy and dissipation fields. The BT eddy results in more contrasting strong and weak energy flux beams of internal tides (Fig. 13a). The strongest beam is formed in the

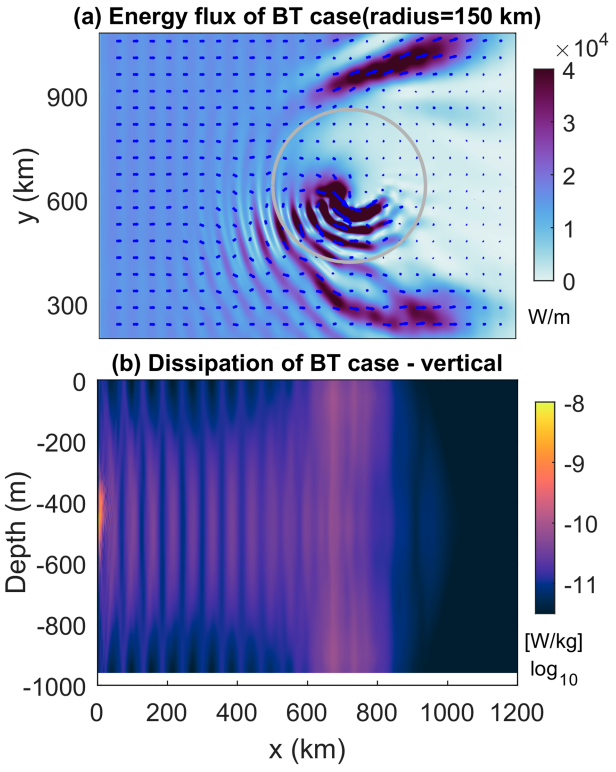

FIG. 13. (a) Depth-integrated and time-averaged baroclinic energy flux of internal tide of the barotropic eddy case (B150). Colors indicate the magnitude and arrows indicate the direction. The gray circles indicate the eddy area with horizontal speed ≥ 0.1 m s^{-1}. (b) Cross section of meridionally averaged (between $y = 450$ km and $y = 830$ km) dissipation rate of the barotropic eddy case (B150). Colors indicate the magnitude.

southern sector of the eddy, close to the eddy core. Part of the incident energy is diverted southwestward, leading to the narrow interference beams. Since the simulation has no depth dependence in the barotropic configuration, the surface enhanced dissipation no longer exists in the BT case (Fig. 13b).

We then compare the high-mode energy flux of BT case (B150) with that of BC case (A150) (Fig. 14). The order of magnitude of mode-2 energy flux density in the eddy region is $\sim 10^1$ W m^{-1} in the BT case, which is more than an order of magnitude weaker than that ($\sim 10^3$ W m^{-1}) of the BC case (Fig. 14a versus Fig. 7a). The mode 3 and higher modes of BT case are all weaker by an order of magnitude than those of the BC case. The comparison suggests that: although the barotropic eddy velocities are able to refract the propagation pattern of the internal tides, the barotropic structure cannot effectively facilitate the energy cascade from low mode to higher modes. Consequently, the high-mode energy in the barotropic eddy is insufficient to sustain enhanced dissipation. This analysis illustrates the fact that the horizontally varying stratification and vertically sheared current in the baroclinic eddy are of crucial importance in cascading the energy to higher modes.

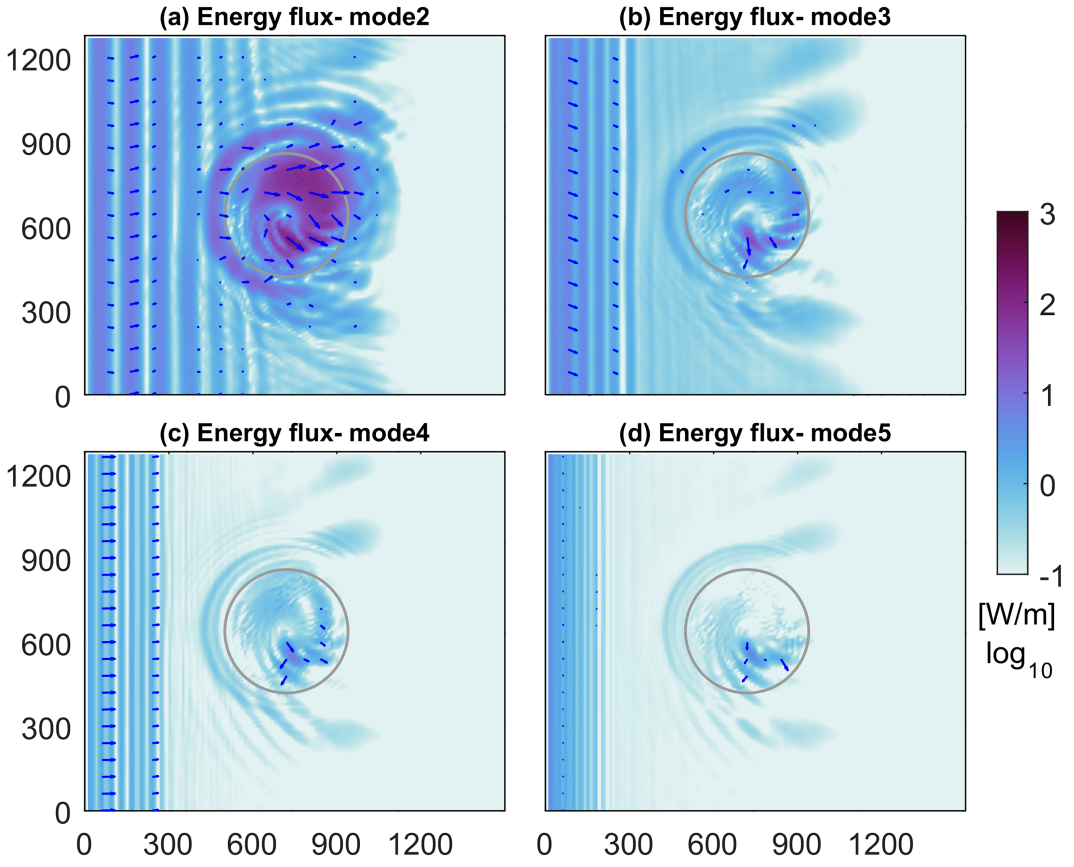

FIG. 14. Horizontal distribution of depth-integrated and time-averaged baroclinic tidal energy flux for barotropic eddy case (B150 case): (a) mode 2, (b) mode 3, (c) mode 4, and (d) mode 5 around day 7. Colors indicate the magnitude of energy flux. Arrows indicate both the direction and magnitude. The gray circles indicate the eddy area with horizontal speed ≥ 0.15 m s^{-1}.

f. Cyclonic eddy case

The results for the cyclonic eddy case (C150) are briefly presented in this subsection. In this experiment, a cyclonic baroclinic eddy with similar scale and magnitude to the 150-km anticyclonic eddy is prescribed for the initial background conditions. Figure 15 shows the energy flux and dissipation cross section of the cyclonic eddy case. Robust energy flux beams are formed in the northern sector of the eddy, with maximum flux density $>$ 35 KW m^{-1}. Some of the energy is even diverted northeastward, interacting with the incident eastward energy to form narrow beams. Notably, an enhanced pattern of dissipation is also found in the cyclonic case. The maximum dissipation rate also reaches $10^{-8.5}$ W kg^{-1}. The dissipation pattern in the vertical is slightly weaker than that in the anticyclonic eddy case (Fig. 15b versus Fig. 3d). The spatial patterns of energy flux and dissipation in the cyclonic case do not show symmetry about the center east–west axis of the eddy with those in the anticyclonic case. This can be primarily attributed to the fact that the structures of the cyclonic eddy and anticyclonic eddy are not simply "identical but of opposite sign," due to the incorporation of centrifugal forces.

The processes and mechanism that cause the enhanced dissipation in the cyclonic eddy are similar to that of the anticyclonic case. The high modes are also effectively generated in the cyclonic eddy case (not shown). Trapping of high modes in the northern sector of cyclonic eddy is then expected to occur. The ray paths for the cyclonic case are also calculated for validation. The mode-1 ray paths coincide well with the simulated energy flux field (Fig. 16a versus Fig. 15a), even reproducing the highly diverted feature in the northern sector of the cyclonic eddy. Once the current is excluded from the ray-tracing calculation, the rays in the cyclonic case can propagate freely through the eddy (Fig. 16c). The mode-2 and mode-3 rays are significantly trapped in the northern eddy sector (Fig. 17).

There are two possible explanations for the different dissipation patterns between anticyclonic and cyclonic cases. First, as previously mentioned, the centrifugal force is included in our eddy initialization and thus the horizontal structures of cyclonic velocity field and anticyclonic field are not completely symmetric. The horizontal gradient of stratification in the cyclonic eddy is different from the anticyclonic case. Consequently, the magnitude of energy transfer between modes should be different. Second, part of the high-mode energy is diverted outward from the northern sector of the cyclonic eddy, forming interference patterns (Fig. 15a), and therefore does not dissipate in the cyclonic eddy region.

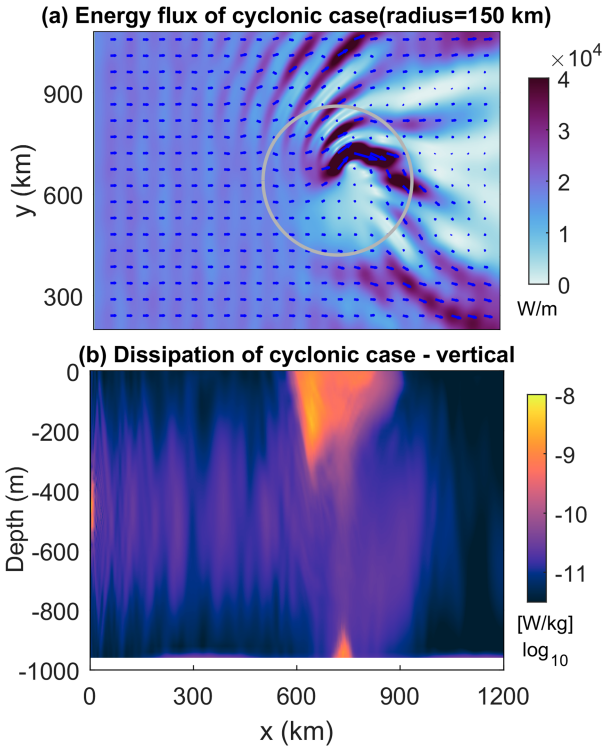

FIG. 15. (a) Depth-integrated and time-averaged baroclinic energy flux of internal tide for the cyclonic eddy case (C150) (eddy radius: 150 km). Colors indicate the magnitude and arrows indicate the direction. The gray circles indicate the eddy area with horizontal speed ≥ 0.1 m s^{-1}. (b) Cross section of meridionally averaged (between $y = 450$ km and $y = 830$ km) dissipation rate of the cyclonic eddy case (C150). Colors indicate the magnitude.

g. *Eddies with different vertical scales*

The dissipation patterns for experiments with different vertical-scale eddies are shown in Fig. 18. One intriguing phenomenon is that the enhanced dissipation in the upper column is further enhanced as the vertical scale is reduced. The dissipation rate reaches a magnitude of 10^{-8} W kg^{-1} in both the 750- and 500-m vertical-scale eddy experiments (Figs. 18c,d). However, the vertical range over which the enhanced dissipation is spreading also decreases as the vertical scale of the eddy decreases. As an example, the enhanced dissipation in the 500-m vertical-scale eddy experiment only extends to about 200-m depth, whereas the enhanced dissipation in the 1000-m vertical-scale eddy case can reach as deep as 400 m (Fig. 18d versus Fig. 3d). Note that the shallower eddy has stronger vertical shear, given that the eddy radius and vorticity remain the same as in the reference case. Possible explanations for the further enhanced dissipation are discussed later.

h. *Sensitivity of dissipation to eddy radius, eddy vorticity, and eddy vertical scale*

To further analyze the sensitivity of dissipation to eddies with different radius, vorticity and vertical scale, the ratio of tidal dissipation (integrated value over the region as indicated by the dashed rectangle in Fig. 3b) in the internal tide–eddy cases to that in the internal tide-only case is presented in Fig. 19. The dissipation of internal tides increases with increasing eddy radius, increasing eddy magnitude (vorticity), and decreasing vertical scale, and the increasing trend with radius appears to be greater than linear (scaling with the eddy area shows a similar trend which is not shown). For example, the internal tide dissipation in the eddy region is approximately 5 times larger in the 150-km eddy case than that in the internal tide-only case. The ratio approaches 10 when the eddy radius increases to 175 km.

The dissipation in low-vorticity eddies is noticeably weaker (blue diamonds in Fig. 19). The lower vorticity corresponds to smaller eddy velocity at the same radius (Table 1). Therefore, we speculate that the reduced trapping effect due to this smaller eddy velocity may explain the weaker dissipation. Ray tracing calculations conducted for the lower-vorticity eddy cases (Cases V002 and V001 in Table 1 with same radius of 150 km but lower vorticity) show that the eddy with vorticity of -2×10^{-5} s^{-1} (V002) is not able to trap the mode-2 internal tides. Although the mode-2 rays are still distorted by the eddy current in the southern sector (Fig. 20a versus Fig. 11b), the mode-2 rays in both sectors can propagate similar distances after 6 days' integration. This eddy can still produce a trapping effect on mode-3 internal tides (Fig. 20b). Nevertheless, mode 3 is approximately one order of magnitude weaker than mode 2 (Fig. 9), so the internal tide dissipation in this case is only slightly increased compared to the internal tide-only simulation. In the case with eddy vorticity of -1×10^{-5} s^{-1} (V001), both mode 2 and mode 3 can freely propagate away from the eddy (Figs. 20c,d), and there is no trapping, explaining the lack of enhanced dissipation.

The increased dissipation of internal tides with decreasing eddy vertical scale can be explained by the increase in the vertical shear of the eddy as the vertical scale decreases, while the eddy radius and vorticity at the surface are held constant. We find that the increased eddy shear leads to more slantwise, high-wavenumber structures of internal tides (Figs. 6e,f), which also possess high shear and thus are more prone to be dissipated. Note that the slantwise high-wavenumber structure cannot be fully reconstructed by adding up the extracted modal components, so as a consequence, modal analysis only indicates a small increase in high-mode energy flux with decreasing eddy vertical scale (not shown). This suggests that under the influence of strong shear, a portion of the generated high-wavenumber energy may be in the form of slantwise vertically propagating structures. This high-wavenumber energy dissipates in the vicinity of the upper eddy and therefore cannot extend over the entire depth to form a modal structure. In some respects, this process is similar to that of traditional bottom generated internal tides and wind-driven near-inertial waves, where part of the energy is dissipated before reaching the surface (internal tides) or bottom (near-inertial waves) for reflection and formation of resonant modes (Shakespeare et al. 2021; Raja et al. 2022).

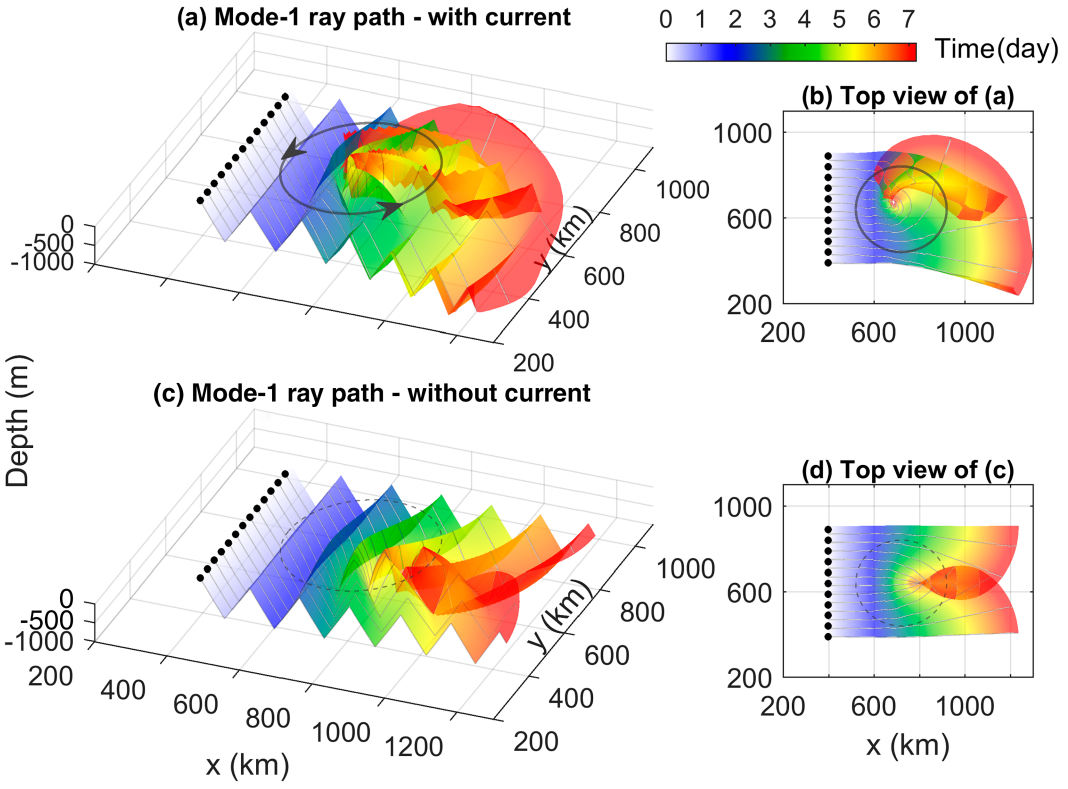

FIG. 16. The 3D ray paths of mode-1 internal tide for the cyclonic eddy case (C150). (a) Computed mode-1 ray paths incorporating both eddy current and stratification. (b) The top view of (a). (c) Computed mode-1 ray paths only incorporating the stratification. (d) Top view of (c). The colors indicate the 3D ray surface and propagation time. The gray lines indicate the ray paths. The gray circles in (a) and (b) indicate the eddy area with horizontal speed ≥ 0.1 m s^{-1}.

4. Discussion

While our simulations have demonstrated internal tide dissipation in baroclinic eddies, we must note some caveats in interpreting these results. The spatial resolutions (2 km horizontal and 20 m vertical) for the present simulation are sufficient to resolve the high-mode internal waves (Buijsman et al. 2014). However, the resolution is insufficient to resolve instability and overturns caused by wave breaking. Performing much higher resolution simulations capable of explicitly resolving the transition to turbulence would require much greater computational resources, given the 3D large domain size and high-frequency output settings. Our simulations do not therefore generate dissipation through a turbulent cascade, but rather the energy loss of internal tides is caused by the dissipation generated by the resolved shear. Previous simulations with similar resolution reported the calculated dissipation compares well with observations in the Indonesian Archipelago (Nagai and Hibiya 2015). Our study aims to understand the mechanisms through which internal tides can transfer energy to small scales, and produce sufficient energy concentration to increase dissipation. Future finer-resolution simulations with nonhydrostatic physics will be necessary to better examine and quantify the details of the dissipation processes. In addition, our simulations have a constant background stratification, whereas the real ocean typically has stronger stratification in the pycnocline. Having now examined this simplified scenario, future simulations will explore the effects associated with more realistic nonuniform stratification.

The eddies employed in the present simulations may be stronger than typically found in the global open ocean. Nevertheless, such eddies may be found in the western boundary current regions or specific circulation systems, such as the Agulhas rings and the Gulf Stream rings (Douglass and Richman 2015; Andres 2016). Low-mode internal tides are much more widespread in the global ocean (Simmons et al. 2004; Arbic et al. 2012; Zhao et al. 2016; Zaron 2019). Duda et al. (2018) found trapping of low-mode internal tides propagating upstream in the Gulf Stream using a 2D ray-tracing method, but few high-mode rays were found to be trapped in mesoscale eddies in their study. A possible reason may be that the high modes in their scenario were generated at the continental shelf region rather than in the eddies, therefore the effect of eddies was not strongly experienced by the high modes.

We use a similar model setting as in Dunphy and Lamb (2014), with mode-1 passing through mesoscale eddies in both studies. Dunphy and Lamb (2014) examined the scattering of mode-1 internal tide energy by the eddy and evaluated the

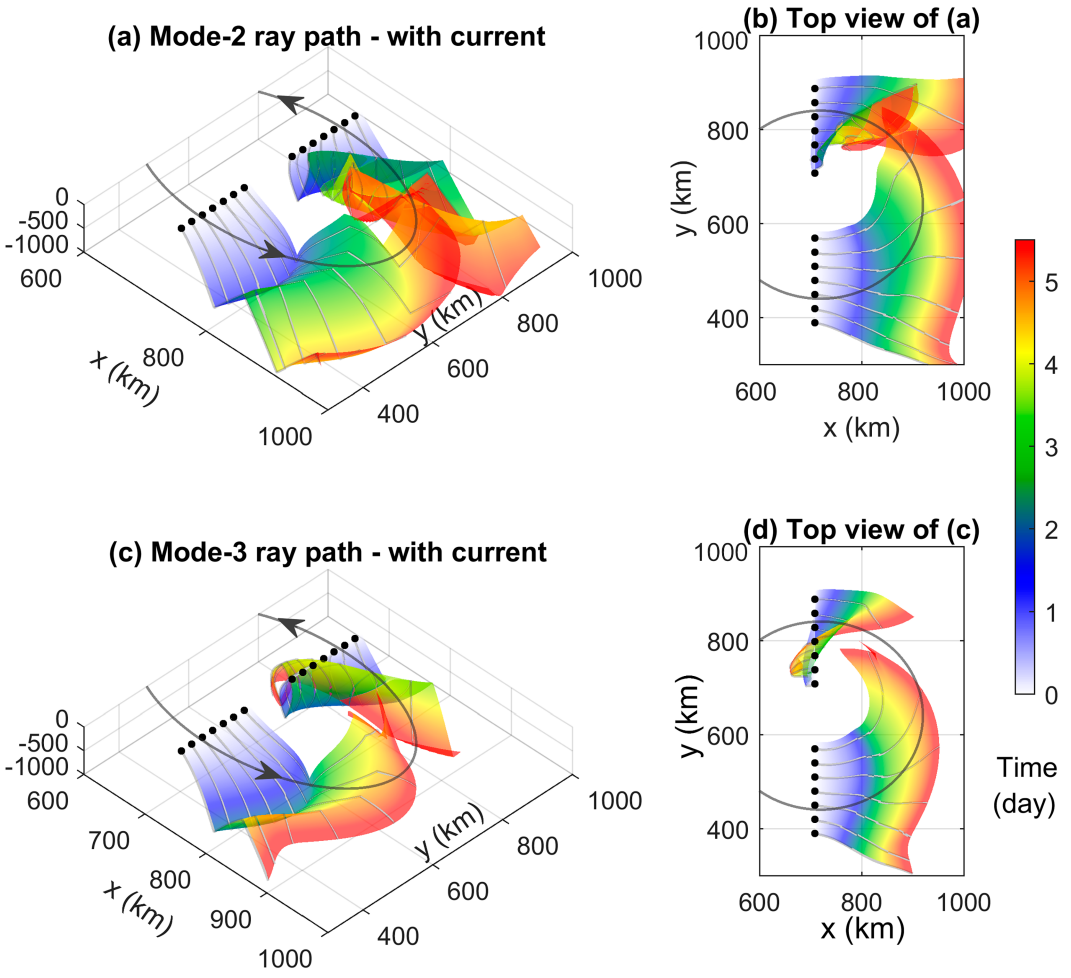

FIG. 17. The 3D ray paths of mode-2 and mode-3 internal tide for the cyclonic eddy case (C150). (a) Computed mode-2 ray paths incorporating both eddy current and stratification. (b) The top view of (a). (c) As in (a), but for mode-3 ray paths. (d) Top view of (c). The black dots represent the initial positions of the rays. The colors indicate the 3D ray surface and propagation time. The gray lines indicate the ray paths. The gray circles in all panels indicate the eddy area with horizontal speed ≥ 0.1 m s^{-1}.

conversion of energy from mode 1 to high modes. The focus of our study is to further investigate whether eddies will affect the dissipation of low-mode internal tides and the underlying mechanisms involved in this enhancement of dissipation. Mesoscale eddies have been shown to enhance the mixing due to near-inertial waves (Whitt and Thomas 2013; Whalen et al. 2018). Dissipation of internal tides in mesoscale eddies, as in this study, may also contribute to local mixing in regions with strong eddies. Our simulations do not have sufficient resolution to investigate this diapycnal mixing, but we speculate that the influence of strong mesoscale currents on the internal tide propagation and dissipation may be associated with tidal mixing which then impacts local water mass transformation and circulation within the eddies (Melet et al. 2013).

Previous studies have been conducted to quantify the transmitted and reflected fraction of internal tides at continental slopes and ridges (Klymak et al. 2011; Sarkar and Scotti 2017). The structure of stratification also plays an important role in onshore internal tide transmission (Liu et al. 2022). The present results also motivate further detailed work to investigate the reflection and transmission processes of internal tides as they propagate through fronts and eddies, which has been discussed in some recent numerical works (Kelly et al. 2016; Dunphy et al. 2017). An accurate depiction of the complicated energy pathway for internal tides in varying mesoscale environments is an important prerequisite for a better estimation of tidal mixing. We also hypothesize that baroclinic eddies can influence tidal dissipation near rough topography, where previous studies have shown that internal tide energy can be effectively transferred from low to high modes (Peacock et al. 2009; Mathur et al. 2014). If the topographically generated high modes become trapped within a baroclinic eddy, dissipation may be enhanced over a broader vertical range than for

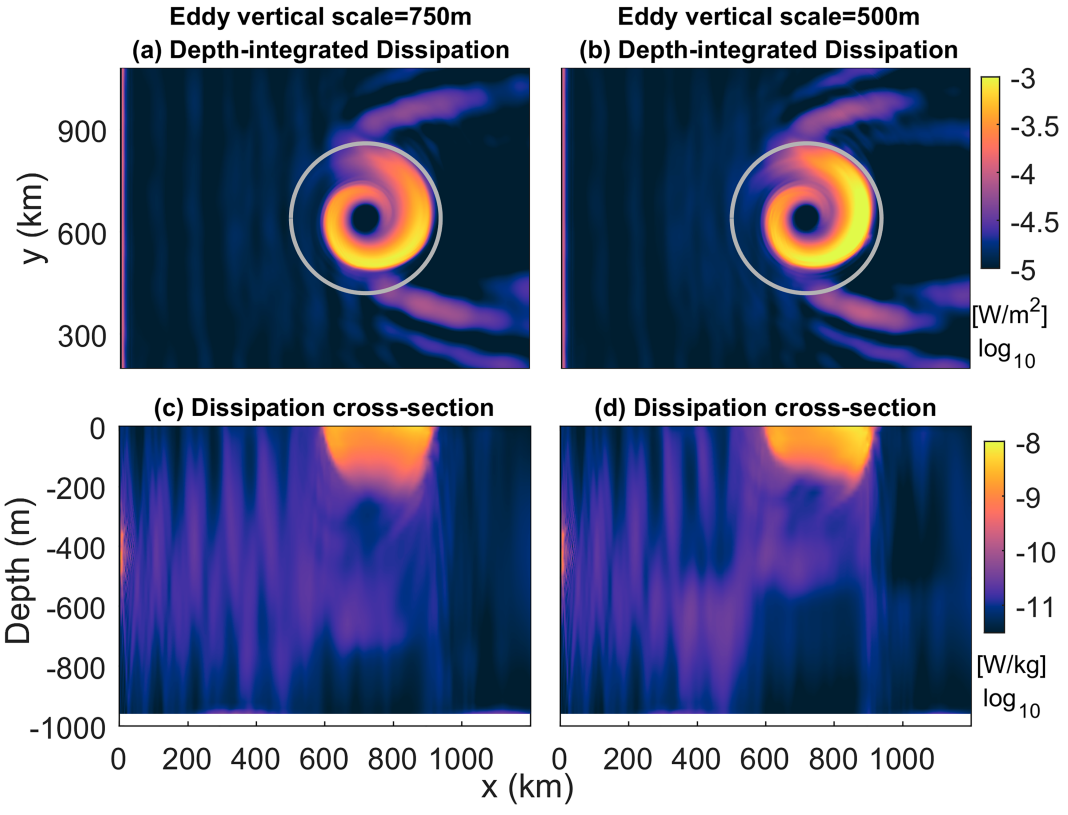

FIG. 18. (a) Depth-integrated and time-averaged tidal dissipation for the 750 m-vertical-scale eddy case (H750). (b) As in (a), but for the 500 m-vertical-scale eddy case (H500). (c) Cross section of meridionally averaged (between $y = 450$ km and $y = 830$ km) dissipation rate for the 750 m-vertical-scale eddy case (H750). (d) As in (c), but for the 500 m-vertical-scale eddy case (H500). Colors indicate the magnitude plotted in log scale. The gray circles indicate the eddy area with horizontal speed ≥ 0.1 m s^{-1}.

topographic scattering alone where internal tide dissipation is concentrated near the bottom (Jayne and St. Laurent 2001; Legg and Klymak 2008; Lefauve et al. 2015; Hibiya et al. 2017). The results of our study provide insights into improving the parameterization of dissipation caused by remotely propagating low-mode internal tides. First, we have confirmed that strong baroclinic eddies act as energy sinks for low-mode internal tides. This information can help in accurately predicting and estimating the internal tide energy available for dissipation at a given location. Second, the surface-intensified dissipation of internal tides in baroclinic eddies can help to provide a better vertical profile of internal tide-driven dissipation.

5. Summary

In this study, we have examined the processes induced by internal tides propagating through baroclinic eddies. We have focused on the dissipation of internal tides within a series of mesoscale eddies that have varying spatial scales and magnitudes. We find enhanced dissipation of internal tides in simulations with strong baroclinic eddies. We have demonstrated that this enhanced dissipation can be attributed to the trapping of high-mode internal waves within the eddy.

The energy flux of mode-1 internal tides is refracted into convergent energy beams that radiate away from the eddy region, resulting in a zone of greatly reduced energy flux in the lee of the eddy (Fig. 2). Enhanced dissipation of the internal tide is found in the strong baroclinic (anticyclonic) eddies, exhibiting an asymmetric pattern with greater dissipation where the eddy velocity opposes the internal wave propagation (Fig. 3) (the southern sector of the eddy in our configuration). The depth-integrated dissipation reaches a maximum magnitude of 10^{-3} W m^{-2} in this region of the eddy. Vertically, the enhanced dissipation is surface intensified in the upper water column, with a maximum magnitude of 10^{-8} W kg^{-1}. The enhanced dissipation rate in the eddy is approximately two orders of magnitude stronger than that in the regions outside of the eddy.

The enhanced dissipation is mainly attributed to the trapped high-mode internal tides. The high modes are effectively generated in the baroclinic eddy. The high modes then experience significant north–south asymmetry in their propagation. The high modes in the southern sector, where internal tides propagate upstream in the eddy current, propagate more slowly than that in the northern sector where eddy velocity and internal tide velocity are in the same direction. As a result, the high

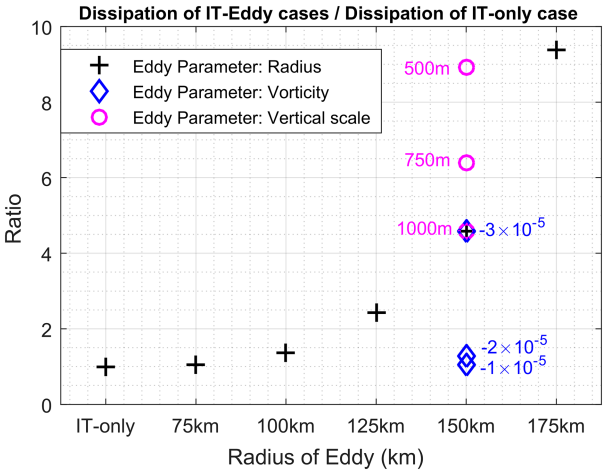

FIG. 19. The ratios of area-integrated dissipation in the internal tide–eddy cases to that in the internal tide-only cases. The cross markers represent the ratios for eddies with different radius with vertical scale of 1000 m and maximum vorticity of -3×10^{-5} s^{-1}. The diamond markers represent ratios for eddies with different maximum vorticity of -3×10^{-5}, -2×10^{-5}, and -1×10^{-5} s^{-1}, respectively. The circle markers represent the ratios for eddies with different vertical scales of 1000, 750, and 500 m, respectively.

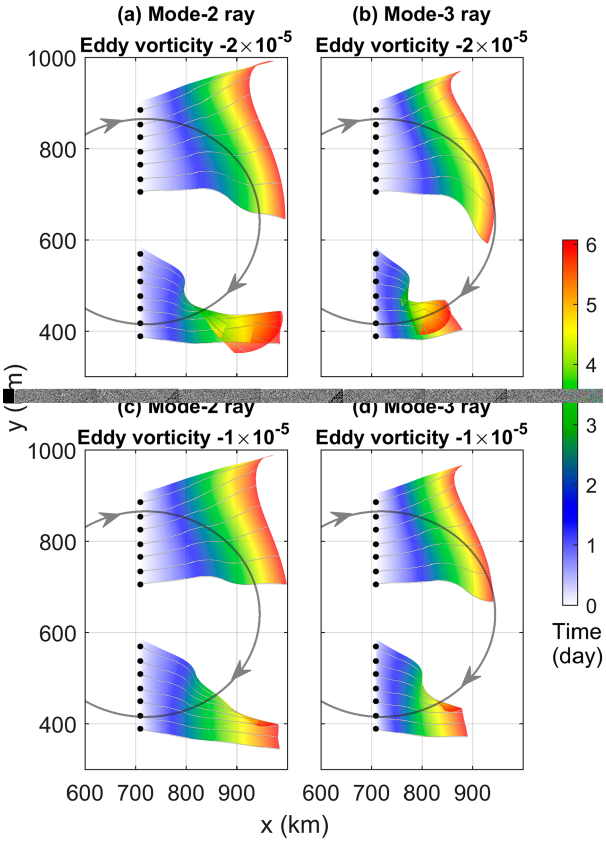

FIG. 20. Top view of 3D ray tracing for the lower-vorticity eddy cases. (a) Computed mode-2 ray paths with incorporating both eddy current and stratification for the eddy with vorticity of -2×10^{-5} s^{-1} (V002). (b) Computed mode-3 ray paths with incorporating both eddy current and stratification for the eddy with vorticity of -2×10^{-5} s^{-1} (V002). (c) As in (a), but for eddy with vorticity of -1×10^{-5} s^{-1} (V001). (d) As in (b), but for eddy with vorticity of -1×10^{-5} s^{-1} (V001). The colors indicate the 3D ray surface and propagation time. The gray lines indicate the ray paths. The gray circles in (a) and (b) indicate the eddy area with horizontal speed ≥ 0.1 m s^{-1}.

modes experience significant trapping in the southern sector. This feature is also revealed in the vertical cross section of the velocity field, where high-wavenumber structures are found in the upper water column in the southern sector of the strong eddy. The slantwise high-wavenumber structures cannot be fully reconstructed by the modal components, indicating that a portion of the generated high-wavenumber energy is in the form of vertically propagating slantwise structures which tend to dissipate along their propagation path.

A 3D theoretical ray-tracing approach is used to further illustrate the trapping processes. The ray-tracing energy pathways generally resemble the modeled energy flux field. Both the mode-2 and mode-3 energy rays in the southern sector of the eddy, where the enhanced dissipation occurs, are substantially trapped. Some of the mode-3 rays are even twisted to propagate westward. A significant finding is that the eddy current plays an essential role in trapping the high modes. Specifically, in the absence of background current, the ray paths show north–south symmetry and no trapped behavior is observed.

Enhanced dissipation of internal tides is also found in the cyclonic eddy case, although the spatial pattern differs. The barotropic eddy is incapable of facilitating robust high modes [where the magnitude of mode 2 reaches the order of $O(0.1)$ of mode 1] and thus cannot generate significant dissipation. The total internal tide dissipation increases with the eddy radius. Since the low-vorticity eddies cannot effectively trap the high modes, the dissipation of internal tides in those cases are much weaker. In cases with reduced eddy vertical scale, the internal tide dissipation is further enhanced, which may be mainly attributed to the increased eddy shear and the resultant slantwise high-wavenumber structures of internal tides.

Acknowledgments. We thank Robert Hallberg for the thoughtful comments and suggestions on this work. We thank Marion Alberty and Henri F. Drake for fruitful scientific discussions. Y.W. is supported by the Outstanding Research Assistant Funding Program of Chinese Academy of Sciences and the National Science Foundation of China (42006031). S.L. is supported by award NA18OAR4320123 from the National Oceanic and Atmospheric Administration, U.S. Department of Commerce. The statements, findings, conclusions, and recommendations are those of the author(s) and do not necessarily reflect the views of the National Oceanic and Atmospheric Administration, or the U.S. Department of Commerce.

Data availability statement. The model setup code and input files used for the simulation in this study are available at Zenodo (doi: 10.5281/zenodo.7693658).

APPENDIX

Sensitivity of Simulation to Dissipation Parameters

A suite of sensitivity experiments is performed to examine how the dissipation parameters impact the energy of internal tides in our simulation (Table A1). Specifically, we conduct the experiments by varying the magnitude of viscosity and diffusivity used in the reference experiment. For each experiment, we calculate the time-averaged and meridionally integrated energy of internal tides along x axis (Fig. A1). The internal tide energy of the reference case along the x axis is indicated by the black line in Fig. A1. Increasing the viscosity and diffusivity by a factor of 10 or larger leads to relatively pronounced energy decay of internal tides compared to the reference experiment (cyan, red, and green lines in Fig. A1). However, the energy decay does not change appreciably in experiments with decreased viscosity and diffusivity (magenta and blue lines in Fig. A1), suggesting that the numerical dissipation is a more significant factor in these simulations. Additionally, the viscosity and diffusivity used in the reference case are large enough to prevent gridscale noise. These results indicate that values of the dissipation parameters ($A_z = K_z = 1 \times 10^{-4}$ m^2 s^{-1} and $A_h = K_h = 1 \times 10^{-1}$ m^2 s^{-1}) used in the simulations for the main body of the study are reasonable, i.e., in a range where dissipation is not sensitive to the precise values, while sufficient to prevent gridscale noise.

TABLE A1. Dissipation parameter settings for the sensitivity experiments. The parameters that were used in the reference experiment and those that were changed in the sensitivity experiments are indicated in bold font.

Expt	Vertical viscosity/ diffusivity (m^2 s^{-1})	Horizontal viscosity/ diffusivity (m^2 s^{-1})
Ref	$\boldsymbol{A_z = K_z = 1 \times 10^{-4}}$	$\boldsymbol{A_h = K_h = 1 \times 10^{-1}}$
1	$\boldsymbol{A_z = K_z = 0.1 \times 10^{-4}}$	$A_h = K_h = 1 \times 10^{-1}$
2	$\boldsymbol{A_z = K_z = 10 \times 10^{-4}}$	$A_h = K_h = 1 \times 10^{-1}$
3	$A_z = K_z = 1 \times 10^{-4}$	$\boldsymbol{A_h = K_h = 0.1 \times 10^{-1}}$
4	$A_z = K_z = 1 \times 10^{-4}$	$\boldsymbol{A_h = K_h = 10 \times 10^{-1}}$
5	$A_z = K_z = 1 \times 10^{-4}$	$\boldsymbol{A_h = K_h = 100 \times 10^{-1}}$

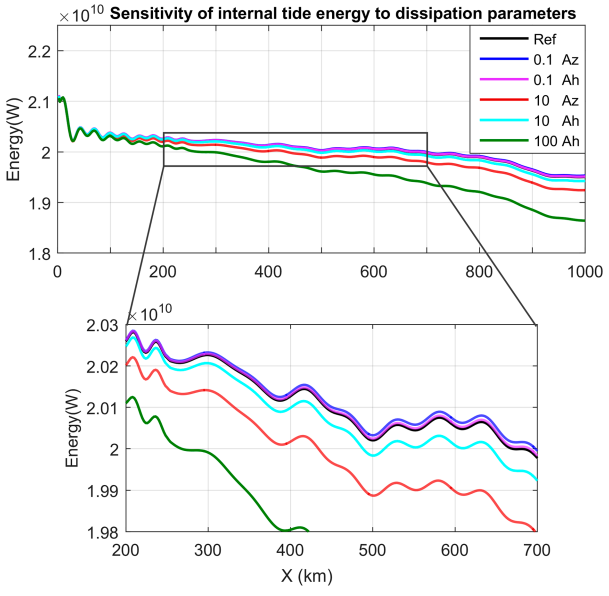

FIG. A1. Time-averaged and meridionally integrated energy of internal tides with respect to varying dissipation parameters. Results of reference case with vertical viscosity A_z and horizontal A_h (black line); experiment with reduced vertical viscosity of $0.1 \times A_z$ (blue line); experiment with reduced horizontal viscosity of $0.1 \times A_h$ (magenta line); experiment with increased vertical viscosity of $10 \times A_z$ (red line); experiment with increased horizontal viscosity of $10 \times A_h$ (cyan line); experiment with increased horizontal viscosity of $100 \times A_h$ (green line).

REFERENCES

Alberty, M. S., S. Billheimer, M. M. Hamann, C. Y. Ou, V. Tamsitt, A. J. Lucas, and M. H. Alford, 2017: A reflecting, steepening, and breaking internal tide in a submarine canyon. *J. Geophys. Res. Oceans*, **122**, 6872–6882, https://doi.org/10.1002/2016JC012583.

Alford, M. H., H. L. Simmons, O. B. Marques, and J. B. Girton, 2019: Internal tide attenuation in the North Pacific. *Geophys. Res. Lett.*, **46**, 8205–8213, https://doi.org/10.1029/2019GL082648.

Andres, M., 2016: On the recent destabilization of the Gulf Stream path downstream of cape Hatteras. *Geophys. Res. Lett.*, **43**, 9836–9842, https://doi.org/10.1002/2016GL069966.

Ansong, J. K., and Coauthors, 2018: Geographical distribution of diurnal and semidiurnal parametric subharmonic instability in a Global Ocean circulation model. *J. Phys. Oceanogr.*, **48**, 1409–1431, https://doi.org/10.1175/JPO-D-17-0164.1.

Arbic, B. K., J. G. Richman, J. F. Shriver, P. G. Timko, E. J. Metzger, and A. J. Wallcraft, 2012: Global modeling of internal tides: Within an eddying ocean general circulation model. *Oceanography*, **25** (2), 20–29, https://doi.org/10.5670/oceanog.2012.38.

Bühler, O., and M. E. McIntyre, 2005: Wave capture and wave–vortex duality. *J. Fluid Mech.*, **534**, 67–95, https://doi.org/10.1017/S0022112005004374.

——, and M. Holmes-Cerfon, 2011: Decay of an internal tide due to random topography in the ocean. *J. Fluid Mech.*, **678**, 271–293, https://doi.org/10.1017/jfm.2011.115.

Buijsman, M. C., S. Legg, and J. Klymak, 2012: Double-ridge internal tide interference and its effect on dissipation in Luzon Strait. *J. Phys. Oceanogr.*, **42**, 1337–1356, https://doi.org/10.1175/JPO-D-11-0210.1.

——, and Coauthors, 2014: Three-dimensional double-ridge internal tide resonance in Luzon Strait. *J. Phys. Oceanogr.*, **44**, 850–869, https://doi.org/10.1175/JPO-D-13-024.1.

——, B. K. Arbic, J. G. Richman, J. F. Shriver, A. J. Wallcraft, and L. Zamudio, 2017: Semidiurnal internal tide incoherence in the equatorial Pacific. *J. Geophys. Res. Oceans*, **122**, 5286–5305, https://doi.org/10.1002/2016JC012590.

——, and Coauthors, 2020: On the interplay between horizontal resolution and wave drag and their effect on tidal baroclinic mode waves in realistic global ocean simulations. *Ocean Modell.*, **152**, 101656, https://doi.org/10.1016/j.ocemod.2020.101656.

Chavanne, C., P. Flament, D. Luther, and K.-W. Gurgel, 2010: The surface expression of semidiurnal internal tides near a strong source at Hawaii. Part II: Interactions with mesoscale

currents. *J. Phys. Oceanogr.*, **40**, 1180–1200, https://doi.org/10.1175/2010JPO4223.1.

Cushman-Roisin, B., and J.-M. Beckers, 2011: *Introduction to Geophysical Fluid Dynamics: Physical and Numerical Aspects*. International Geophysics Series, Vol. 101, Academic Press, 828 pp.

de Lavergne, C., and Coauthors, 2020: A parameterization of local and remote tidal mixing. *J. Adv. Model. Earth Syst.*, **12**, e2020MS002065, https://doi.org/10.1029/2020MS002065.

Douglass, E. M., and J. G. Richman, 2015: Analysis of ageostrophy in strong surface eddies in the Atlantic Ocean. *J. Geophys. Res. Oceans*, **120**, 1490–1507, https://doi.org/10.1002/2014JC010350.

Duda, T. F., Y.-T. Lin, M. Buijsman, and A. E. Newhall, 2018: Internal tidal modal ray refraction and energy ducting in baroclinic Gulf Stream currents. *J. Phys. Oceanogr.*, **48**, 1969–1993, https://doi.org/10.1175/JPO-D-18-0031.1.

Dunphy, M., and K. G. Lamb, 2014: Focusing and vertical mode scattering of the first mode internal tide by mesoscale eddy interaction. *J. Geophys. Res. Oceans*, **119**, 523–536, https://doi.org/10.1002/2013JC009293.

——, A. L. Ponte, P. Klein, and S. Le Gentil, 2017: Low-mode internal tide propagation in a turbulent eddy field. *J. Phys. Oceanogr.*, **47**, 649–665, https://doi.org/10.1175/JPO-D-16-0099.1.

Egbert, G. D., and R. D. Ray, 2000: Significant dissipation of tidal energy in the deep ocean inferred from satellite altimeter data. *Nature*, **405**, 775–778, https://doi.org/10.1038/35015531.

Falahat, S., J. Nycander, F. Roquet, and M. Zarroug, 2014: Global calculation of tidal energy conversion into vertical normal modes. *J. Phys. Oceanogr.*, **44**, 3225–3244, https://doi.org/10.1175/JPO-D-14-0002.1.

Gill, A. E., 1982: *Atmosphere-Ocean Dynamics*. International Geophysics Series, Vol. 30, Academic Press, 662 pp.

Hall, R. A., J. M. Huthnance, and R. G. Williams, 2013: Internal wave reflection on shelf slopes with depth-varying stratification. *J. Phys. Oceanogr.*, **43**, 248–258, https://doi.org/10.1175/JPO-D-11-0192.1.

Hibiya, T., M. Nagasawa, and Y. Niwa, 2002: Nonlinear energy transfer within the oceanic internal wave spectrum at mid and high latitudes. *J. Geophys. Res.*, **107**, 3207, https://doi.org/10.1029/2001JC001210.

——, T. Ijichi, and R. Robertson, 2017: The impacts of ocean bottom roughness and tidal flow amplitude on abyssal mixing. *J. Geophys. Res. Oceans*, **122**, 5645–5651, https://doi.org/10.1002/2016JC012564.

Huang, X., Z. Wang, Z. Zhang, Y. Yang, C. Zhou, Q. Yang, W. Zhao, and J. Tian, 2018: Role of mesoscale eddies in modulating the semidiurnal internal tide: Observation results in the northern South China Sea. *J. Phys. Oceanogr.*, **48**, 1749–1770, https://doi.org/10.1175/JPO-D-17-0209.1.

Jayne, S. R., and L. C. St. Laurent, 2001: Parameterizing tidal dissipation over rough topography. *Geophys. Res. Lett.*, **28**, 811–814, https://doi.org/10.1029/2000GL012044.

Jing, Z., P. Chang, S. F. DiMarco, and L. Wu, 2018: Observed energy exchange between low-frequency flows and internal waves in the Gulf of Mexico. *J. Phys. Oceanogr.*, **48**, 995–1008, https://doi.org/10.1175/JPO-D-17-0263.1.

Johnston, T. M. S., M. A. Merrifield, and P. E. Holloway, 2003: Internal tide scattering at the Line Islands ridge. *J. Geophys. Res.*, **108**, 3365, https://doi.org/10.1029/2003JC001844.

Jones, R. M., 2005: A general dispersion relation for internal gravity waves in the atmosphere or ocean, including baroclinicity, vorticity, and rate of strain. *J. Geophys. Res.*, **110**, D22106, https://doi.org/10.1029/2004JD005654.

Jones, W. L., 1969: Ray tracing for internal gravity waves. *J. Geophys. Res.*, **74**, 2028–2033, https://doi.org/10.1029/JB074i008p02028.

Kang, D., and O. Fringer, 2012: Energetics of barotropic and baroclinic tides in the Monterey Bay area. *J. Phys. Oceanogr.*, **42**, 272–290, https://doi.org/10.1175/JPO-D-11-039.1.

Kelly, S. M., J. D. Nash, K. I. Martini, M. H. Alford, and E. Kunze, 2012: The cascade of tidal energy from low to high modes on a continental slope. *J. Phys. Oceanogr.*, **42**, 1217–1232, https://doi.org/10.1175/JPO-D-11-0231.1.

——, P. F. Lermusiaux, T. F. Duda, and P. J. Haley Jr., 2016: A coupled-mode shallow-water model for tidal analysis: Internal tide reflection and refraction by the Gulf Stream. *J. Phys. Oceanogr.*, **46**, 3661–3679, https://doi.org/10.1175/JPO-D-16-0018.1.

Klymak, J. M., R. Pinkel, and L. Rainville, 2008: Direct breaking of the internal tide near topography: Kaena Ridge, Hawaii. *J. Phys. Oceanogr.*, **38**, 380–399, https://doi.org/10.1175/2007JPO3728.1.

——, M. H. Alford, R. Pinkel, R.-C. Lien, Y. J. Yang, and T.-Y. Tang, 2011: The breaking and scattering of the internal tide on a continental slope. *J. Phys. Oceanogr.*, **41**, 926–945, https://doi.org/10.1175/2010JPO4500.1.

——, H. L. Simmons, D. Braznikov, S. Kelly, J. A. MacKinnon, M. H. Alford, R. Pinkel, and J. D. Nash, 2016: Reflection of linear internal tides from realistic topography: The Tasman continental slope. *J. Phys. Oceanogr.*, **46**, 3321–3337, https://doi.org/10.1175/JPO-D-16-0061.1.

Knox, J. A., and P. R. Ohmann, 2006: Iterative solutions of the gradient wind equation. *Comput. Geosci.*, **32**, 656–662, https://doi.org/10.1016/j.cageo.2005.09.009.

Koch-Larrouy, A., G. Madec, P. Bouruet-Aubertot, T. Gerkema, L. Bessières, and R. Molcard, 2007: On the transformation of Pacific Water into Indonesian Throughflow Water by internal tidal mixing. *Geophys. Res. Lett.*, **34**, L04604, https://doi.org/10.1029/2006GL028405.

Kunze, E., 1985: Near-inertial wave propagation in geostrophic shear. *J. Phys. Oceanogr.*, **15**, 544–565, https://doi.org/10.1175/1520-0485(1985)015<0544:NIWPIG>2.0.CO;2.

Lefauve, A., C. Muller, and A. Melet, 2015: A three-dimensional map of tidal dissipation over abyssal hills. *J. Geophys. Res. Oceans*, **120**, 4760–4777, https://doi.org/10.1002/2014JC010598.

Legg, S., 2004: Internal tides generated on a corrugated continental slope. Part I: Cross-slope barotropic forcing. *J. Phys. Oceanogr.*, **34**, 156–173, https://doi.org/10.1175/1520-0485(2004)034<0156:ITGOAC>2.0.CO;2.

——, 2014: Scattering of low-mode internal waves at finite isolated topography. *J. Phys. Oceanogr.*, **44**, 359–383, https://doi.org/10.1175/JPO-D-12-0241.1.

——, and A. Adcroft, 2003: Internal wave breaking at concave and convex continental slopes. *J. Phys. Oceanogr.*, **33**, 2224–2246, https://doi.org/10.1175/1520-0485(2003)033<2224:IWBACA>2.0.CO;2.

——, and J. Klymak, 2008: Internal hydraulic jumps and overturning generated by tidal flow over a tall steep ridge. *J. Phys. Oceanogr.*, **38**, 1949–1964, https://doi.org/10.1175/2008JPO3777.1.

Lelong, M.-P., and J. J. Riley, 1991: Internal wave—Vortical mode interactions in strongly stratified flows. *J. Fluid Mech.*, **232**, 1–19, https://doi.org/10.1017/S0022112091003609.

Liu, Z., W. G. Zhang, and K. R. Helfrich, 2022: Vertical structure of barotropic-to-baroclinic tidal energy conversion on a continental slope. *J. Geophys. Res. Oceans*, **127**, e2022JC019130, https://doi.org/10.1029/2022JC019130.

Löb, J., J. Köhler, C. Mertens, M. Walter, Z. Li, J.-S. von Storch, Z. Zhao, and M. Rhein, 2020: Observations of the low-mode internal tide and its interaction with mesoscale flow south of the Azores. *J. Geophys. Res. Oceans*, **125**, e2019JC015879, https://doi.org/10.1029/2019JC015879.

MacKinnon, J., 2013: Mountain waves in the deep ocean. *Nature*, **501**, 321–322, https://doi.org/10.1038/501321a.

MacKinnon, J. A., and Coauthors, 2017: Climate process team on internal wave–driven ocean mixing. *Bull. Amer. Meteor. Soc.*, **98**, 2429–2454, https://doi.org/10.1175/BAMS-D-16-0030.1.

Marshall, J., A. Adcroft, C. Hill, L. Perelman, and C. Heisey, 1997: A finite-volume, incompressible Navier Stokes model for studies of the ocean on parallel computers. *J. Geophys. Res.*, **102**, 5753–5766, https://doi.org/10.1029/96JC02775.

Martini, K. I., M. H. Alford, E. Kunze, S. M. Kelly, and J. D. Nash, 2011: Observations of internal tides on the Oregon continental slope. *J. Phys. Oceanogr.*, **41**, 1772–1794, https://doi.org/10.1175/2011JPO4581.1.

Mathur, M., G. S. Carter, and T. Peacock, 2014: Topographic scattering of the low-mode internal tide in the deep ocean. *J. Geophys. Res. Oceans*, **119**, 2165–2182, https://doi.org/10.1002/2013JC009152.

Melet, A., R. Hallberg, S. Legg, and K. Polzin, 2013: Sensitivity of the ocean state to the vertical distribution of internal-tide-driven mixing. *J. Phys. Oceanogr.*, **43**, 602–615, https://doi.org/10.1175/JPO-D-12-055.1.

——, S. Legg, and R. Hallberg, 2016: Climatic impacts of parameterized local and remote tidal mixing. *J. Climate*, **29**, 3473–3500, https://doi.org/10.1175/JCLI-D-15-0153.1.

Merrifield, M. A., P. E. Holloway, and T. M. S. Johnston, 2001: The generation of internal tides at the Hawaiian ridge. *Geophys. Res. Lett.*, **28**, 559–562, https://doi.org/10.1029/2000GL011749.

Molodtsov, S., A. Anis, R. M. W. Amon, and P. Perez-Brunius, 2020: Turbulent mixing in a loop current eddy from glider-based microstructure observations. *Geophys. Res. Lett.*, **47**, e2020GL088033, https://doi.org/10.1029/2020GL088033.

Munk, W., and C. Wunsch, 1998: Abyssal recipes II: Energetics of tidal and wind mixing. *Deep-Sea Res. I*, **45**, 1977–2010, https://doi.org/10.1016/S0967-0637(98)00070-3.

Nagai, T., and T. Hibiya, 2015: Internal tides and associated vertical mixing in the Indonesian archipelago. *J. Geophys. Res. Oceans*, **120**, 3373–3390, https://doi.org/10.1002/2014JC010592.

Nash, J. D., E. Kunze, J. M. Toole, and R. W. Schmitt, 2004: Internal tide reflection and turbulent mixing on the continental slope. *J. Phys. Oceanogr.*, **34**, 1117–1134, https://doi.org/10.1175/1520-0485(2004)034<1117:ITRATM>2.0.CO;2.

——, ——, C. M. Lee, and T. B. Sanford, 2006: Structure of the baroclinic tide generated at Kaena Ridge, Hawaii. *J. Phys. Oceanogr.*, **36**, 1123–1135, https://doi.org/10.1175/JPO2883.1.

Nazarian, R. H., and S. Legg, 2017: Internal wave scattering in continental slope canyons, part 1: Theory and development of a ray tracing algorithm. *Ocean Modell.*, **118**, 1–15, https://doi.org/10.1016/j.ocemod.2017.07.002.

Nikurashin, M., and S. Legg, 2011: A mechanism for local dissipation of internal tides generated at rough topography. *J. Phys. Oceanogr.*, **41**, 378–395, https://doi.org/10.1175/2010JPO4522.1.

Niwa, Y., and T. Hibiya, 2004: Three-dimensional numerical simulation of M_2 internal tides in the East China Sea. *J. Geophys. Res.*, **109**, C04027, https://doi.org/10.1029/2003JC001923.

Nycander, J., 2005: Generation of internal waves in the deep ocean by tides. *J. Geophys. Res.*, **110**, C10028, https://doi.org/10.1029/2004JC002487.

Olbers, D. J., 1981: The propagation of internal waves in a geostrophic current. *J. Phys. Oceanogr.*, **11**, 1224–1233, https://doi.org/10.1175/1520-0485(1981)011<1224:TPOIWI>2.0.CO;2.

——, F. Pollmann, and C. Eden, 2020: On PSI interactions in internal gravity wave fields and the decay of baroclinic tides. *J. Phys. Oceanogr.*, **50**, 751–771, https://doi.org/10.1175/JPO-D-19-0224.1.

Peacock, T., M. J. Mercier, H. Didelle, S. Viboud, and T. Dauxois, 2009: A laboratory study of low-mode internal tide scattering by finite-amplitude topography. *Phys. Fluids*, **21**, 121702, https://doi.org/10.1063/1.3267096.

Polzin, K. L., 2010: Mesoscale eddy–internal wave coupling. Part II: Energetics and results from PolyMode. *J. Phys. Oceanogr.*, **40**, 789–801, https://doi.org/10.1175/2009JPO4039.1.

——, J. M. Toole, and R. W. Schmitt, 1995: Finescale parameterizations of turbulent dissipation. *J. Phys. Oceanogr.*, **25**, 306–328, https://doi.org/10.1175/1520-0485(1995)025<0306:FPOTD>2.0.CO;2.

Ponte, A. L., and P. Klein, 2015: Incoherent signature of internal tides on sea level in idealized numerical simulations. *Geophys. Res. Lett.*, **42**, 1520–1526, https://doi.org/10.1002/2014GL062583.

Rainville, L., and R. Pinkel, 2006: Propagation of low-mode internal waves through the ocean. *J. Phys. Oceanogr.*, **36**, 1220–1236, https://doi.org/10.1175/JPO2889.1.

Raja, K. J., M. C. Buijsman, J. F. Shriver, B. K. Arbic, and O. Siyanbola, 2022: Near-inertial wave energetics modulated by background flows in a global model simulation. *J. Phys. Oceanogr.*, **52**, 823–840, https://doi.org/10.1175/JPO-D-21-0130.1.

Sarkar, S., and A. Scotti, 2017: From topographic internal gravity waves to turbulence. *Annu. Rev. Fluid Mech.*, **49**, 195–220, https://doi.org/10.1146/annurev-fluid-010816-060013.

Savage, A. C., A. F. Waterhouse, and S. M. Kelly, 2020: Internal tide nonstationarity and wave–mesoscale interactions in the Tasman Sea. *J. Phys. Oceanogr.*, **50**, 2931–2951, https://doi.org/10.1175/JPO-D-19-0283.1.

Shakespeare, C. J., B. K. Arbic, and A. M. Hogg, 2021: Dissipating and reflecting internal waves. *J. Phys. Oceanogr.*, **51**, 2517–2531.

Sheen, K. L., and Coauthors, 2014: Eddy-induced variability in Southern Ocean abyssal mixing on climatic timescales. *Nat. Geosci.*, **7**, 577–582, https://doi.org/10.1038/ngeo2200.

Simmons, H. L., R. W. Hallberg, and B. K. Arbic, 2004: Internal wave generation in a global baroclinic tide model. *Deep-Sea Res. II*, **51**, 3043–3068, https://doi.org/10.1016/j.dsr2.2004.09.015.

Smith, S. G. L., and W. R. Young, 2002: Conversion of the barotropic tide. *J. Phys. Oceanogr.*, **32**, 1554–1566, https://doi.org/10.1175/1520-0485(2002)032<1554:COTBT>2.0.CO;2.

St. Laurent, L. C., H. L. Simmons, and S. R. Jayne, 2002: Estimating tidally driven mixing in the deep ocean. *Geophys. Res. Lett.*, **29**, 2106, https://doi.org/10.1029/2002GL015633.

Sun, O. M., and R. Pinkel, 2013: Subharmonic energy transfer from the semidiurnal internal tide to near-diurnal motions over Kaena Ridge, Hawaii. *J. Phys. Oceanogr.*, **43**, 766–789, https://doi.org/10.1175/JPO-D-12-0141.1.

Tabaei, A., T. Akylas, and K. G. Lamb, 2005: Nonlinear effects in reflecting and colliding internal wave beams. *J. Fluid Mech.*, **526**, 217–243, https://doi.org/10.1017/S0022112004002769.

Thorpe, S., 2018: Models of energy loss from internal waves breaking in the ocean. *J. Fluid Mech.*, **836**, 72–116, https://doi.org/10.1017/jfm.2017.780.

Vic, C., and Coauthors, 2019: Deep-ocean mixing driven by small-scale internal tides. *Nat. Commun.*, **10**, 2099, https://doi.org/10.1038/s41467-019-10149-5.

Wang, Y., Z. Xu, B. Yin, Y. Hou, and H. Chang, 2018: Long-range radiation and interference pattern of multisource M_2 internal tides in the Philippine Sea. *J. Geophys. Res. Oceans*, **123**, 5091–5112, https://doi.org/10.1029/2018JC013910.

——, ——, T. Hibiya, B. Yin, and F. Wang, 2021: Radiation path of diurnal internal tides in the northwestern Pacific controlled by refraction and interference. *J. Geophys. Res. Oceans*, **126**, e2020JC016972, https://doi.org/10.1029/2020JC016972.

Whalen, C. B., J. A. MacKinnon, and L. D. Talley, 2018: Large-scale impacts of the mesoscale environment on mixing from wind-driven internal waves. *Nat. Geosci.*, **11**, 842–847, https://doi.org/10.1038/s41561-018-0213-6.

Whitt, D. B., and L. N. Thomas, 2013: Near-inertial waves in strongly baroclinic currents. *J. Phys. Oceanogr.*, **43**, 706–725, https://doi.org/10.1175/JPO-D-12-0132.1.

Zaron, E. D., 2019: Baroclinic tidal sea level from exact-repeat mission altimetry. *J. Phys. Oceanogr.*, **49**, 193–210, https://doi.org/10.1175/JPO-D-18-0127.1.

——, and G. D. Egbert, 2014: Time-variable refraction of the internal tide at the Hawaiian ridge. *J. Phys. Oceanogr.*, **44**, 538–557, https://doi.org/10.1175/JPO-D-12-0238.1.

Zhang, Z., W. Wang, and B. Qiu, 2014: Oceanic mass transport by mesoscale eddies. *Science*, **345**, 322–324, https://doi.org/10.1126/science.1252418.

Zhao, Z., and M. H. Alford, 2009: New altimetric estimates of mode-1 M_2 internal tides in the central North Pacific Ocean. *J. Phys. Oceanogr.*, **39**, 1669–1684, https://doi.org/10.1175/2009JPO3922.1.

——, ——, J. A. MacKinnon, and R. Pinkel, 2010: Long-range propagation of the semidiurnal internal tide from the Hawaiian ridge. *J. Phys. Oceanogr.*, **40**, 713–736, https://doi.org/10.1175/2009JPO4207.1.

——, ——, J. B. Girton, L. Rainville, and H. L. Simmons, 2016: Global observations of open-ocean mode-1 M_2 internal tides. *J. Phys. Oceanogr.*, **46**, 1657–1684, https://doi.org/10.1175/JPO-D-15-0105.1.